

INFORMATION TO USERS

This was produced from a copy of a document sent to us for microfilming. While the most advanced technological means to photograph and reproduce this document have been used, the quality is heavily dependent upon the quality of the material submitted.

The following explanation of techniques is provided to help you understand markings or notations which may appear on this reproduction.

1. The sign or "target" for pages apparently lacking from the document photographed is "Missing Page(s)". If it was possible to obtain the missing page(s) or section, they are spliced into the film along with adjacent pages. This may have necessitated cutting through an image and duplicating adjacent pages to assure you of complete continuity.
2. When an image on the film is obliterated with a round black mark it is an indication that the film inspector noticed either blurred copy because of movement during exposure, or duplicate copy. Unless we meant to delete copyrighted materials that should not have been filmed, you will find a good image of the page in the adjacent frame. If copyrighted materials were deleted you will find a target note listing the pages in the adjacent frame.
3. When a map, drawing or chart, etc., is part of the material being photographed the photographer has followed a definite method in "sectioning" the material. It is customary to begin filming at the upper left hand corner of a large sheet and to continue from left to right in equal sections with small overlaps. If necessary, sectioning is continued again—beginning below the first row and continuing on until complete.
4. For any illustrations that cannot be reproduced satisfactorily by xerography, photographic prints can be purchased at additional cost and tipped into your xerographic copy. Requests can be made to our Dissertations Customer Services Department.
5. Some pages in any document may have indistinct print. In all cases we have filmed the best available copy.

University
Microfilms
International

300 N. ZEEB RD., ANN ARBOR, MI 48106

8128858

SEVERIN, C. SHERMAN

NEW AMORPHOUS MAGNETIC MATERIALS OF IRON-BORON-
BERYLLIUM AND IRON-BORON-GOLD

Iowa State University

PH.D. 1981

**University
Microfilms
International** 300 N. Zeeb Road, Ann Arbor, MI 48106

PLEASE NOTE:

In all cases this material has been filmed in the best possible way from the available copy. Problems encountered with this document have been identified here with a check mark .

1. Glossy photographs or pages _____
2. Colored illustrations, paper or print _____
3. Photographs with dark background _____
4. Illustrations are poor copy _____
5. Pages with black marks, not original copy _____
6. Print shows through as there is text on both sides of page _____
7. Indistinct, broken or small print on several pages
8. Print exceeds margin requirements _____
9. Tightly bound copy with print lost in spine _____
10. Computer printout pages with indistinct print _____
11. Page(s) _____ lacking when material received, and not available from school or author.
12. Page(s) _____ seem to be missing in numbering only as text follows.
13. Two pages numbered _____. Text follows.
14. Curling and wrinkled pages _____
15. Other _____

**University
Microfilms
International**

New amorphous magnetic materials of Fe-B-Be and Fe-B-Au

by

C. Sherman Severin

**A Dissertation Submitted to the
Graduate Faculty in Partial Fulfillment of the
Requirements for the Degree of
DOCTOR OF PHILOSOPHY**

**Department: Materials Science and Engineering
Major: Metallurgy**

Approved:

Signature was redacted for privacy.

In Charge of Major Work

Signature was redacted for privacy.

For the Major Department

Signature was redacted for privacy.

For the Graduate College

**Iowa State University
Ames, Iowa**

1981

TABLE OF CONTENTS

	Page
I. INTRODUCTION	1
A. Fe-B-Be	3
B. Fe-B-Au	7
C. Structural Study	8
II. EXPERIMENTAL PROCEDURE	10
III. DATA REDUCTION METHOD FOR RADIAL DISTRIBUTION FUNCTIONS	18
IV. RESULTS AND DISCUSSION	23
A. Fe-B-Be	23
1. Magnetic and thermomagnetic behavior	23
2. Auger electronic spectroscopy as a probe of the electronic structure	28
3. Mössbauer spectroscopy	34
a. Hyperfine-field distribution and isomer shift	34
b. Crystallization products	42
4. A discussion of charge transfer and the magnetic moment	48
B. Fe-B-Au	52
1. Magnetic and thermomagnetic behavior	52
2. Crystallization of $\text{Fe}_{87}\text{B}_{11}\text{Au}_2$	63
C. Atomic Arrangement Based on Radial Distribution Functions	65
1. $\text{Fe}_{87}\text{B}_{13}$	65
2. $\text{Fe}_{82}\text{B}_{12}\text{C}_6$ and $\text{Fe}_{82}\text{B}_{12}\text{Si}_6$	69
3. $\text{Fe}_{82}\text{B}_{14}\text{Be}_4$ and $\text{Fe}_{82}\text{B}_{13}\text{Be}_5$	75
V. SUMMARY AND CONCLUSIONS	80
VI. BIBLIOGRAPHY	83
VII. ACKNOWLEDGMENTS	88

I. INTRODUCTION

Amorphous materials are noncrystalline material in which long-range crystalline atomic arrangements are absent. The amorphous state in most materials is actually a nonequilibrium configuration resulting from a destabilization of the crystalline state and therefore, the amorphous state is less stable than the crystalline phase. Although there is no long-range order in the amorphous materials, there are characteristic short-range atomic arrangements with preferential bonding. These arrangements are manifested as broad maxima in the X-ray diffraction pattern in which the one or more broad peaks emerge as a result of the distribution of the nearest neighbor atoms which varies with interatomic distances and the atomic size. (This is the basis which enables one to obtain structural information in a radial distribution function analysis.)

The transformation of an amorphous solid to the crystalline state is usually a two-step process. The material first transforms to a reversible glassy state which resembles a frozen liquid. At the amorphous-to-glassy transition temperature a large change in the specific heat and in the coefficient of thermal expansion is usually observed. A further increase in temperature produces the crystalline state irreversibly.

The amorphous materials have been attracting a great deal of attention in the last decade because of their novelty and application potential. In this work, we have concentrated on metallic glasses which are amorphous alloys containing metals and glass-forming elements like B, C, Si, Ge, and P, the so-called metalloids. The Fe-base metallic glasses are of special interest because they are considered as candidates

for the replacement of the crystalline Fe-Si sheets used in power transformers. The metallic glasses are more ductile and can be prepared in the form of 2-5 cm wide ribbons suitable for winding into a transformer core. Also, the rapid quenching technique normally used to produce amorphous materials has been used to produce crystalline 6.5% Si-Fe which is more ductile than that produced by the conventional casting and rolling method. The higher electrical resistivity of the metallic glasses results in lower eddy-current losses.

The one step fabrication (direct casting) of the metallic glass ribbons makes them very attractive from an economic standpoint. This eliminates the forging, rolling, annealing, and drawing steps which usually follow the casting of a crystalline ingot in the usual method of producing transformer material.

Unfortunately, the Fe-base metallic glasses have lower saturation induction when compared to those of crystalline Fe-Si alloys. There is also a corresponding decrease in the average Fe magnetic moment in the Fe-base metallic glasses and this has been attributed to a transfer of electrons from the metalloid atoms to the split d-band of Fe. Therefore, there are two approaches that could be taken to investigate the problem of low saturation induction. First, the charge transfer model could be examined, and if it is valid, lower valence glass-forming elements could be alloyed with Fe. Secondly, the initial moment of Fe could be sufficiently high that the deleterious effect of the glass-forming nonmagnetic elements on the saturation induction will not be significant enough to preclude the use of such alloys in the electrical devices. In this study, we followed the first approach by partially replacing B in Fe-B by Be and

by Au; the second approach was followed also by the use of Au which is known to cause an increase in the average Fe moment. Another aspect of this work, outside of the attempt to attain higher saturation inductions for applications in electrical devices, was to furnish information on the basic understanding of the magnetic interactions, the stability of the amorphous state and the atomic arrangements in several important Fe-base metallic glasses. The report which follows is divided into three parts: (I) the work on Fe-B-Be alloys, (II) the magnetic and annealing behavior of Fe-B-Au alloys, and (III) the structural radial distribution function analyses on Fe-B-Be, Fe-B-Si, and Fe-B-C metallic glasses. More specific introductory remarks on each of these three topics are given below.

A. Fe-B-Be

The low coercive force and low eddy-current losses observed in Fe-base metallic glasses have aroused considerable interest in these materials. However, one of the impeding factors in the potential use of the Fe-metalloid (B, P, C, Si and Ge) amorphous alloys to replace crystalline Fe-Si alloys in power transformers is their lower saturation inductions. This deficiency has its origin in the decrease of the Fe moment because of the presence of the metalloids. For example, in the typical alloy $\text{Fe}_{100-x}(\text{M}, \text{M}')_x$, where M and M' are two metalloids, both B and P cause a reduction in the Fe moment, with P being more adverse than B (1). A similar effect had been observed in the crystalline transition-metal monoborides, and Lundquist et al. (2) have proposed a charge transfer model based on a rigid band concept to explain the reduction of the Fe moment. Within this model, the reduced TM (Fe, Co, Ni) moment is

attributed to the filling-in of the vacant states in the d band of the TM by electrons transferred from the p states of the metalloids. When this model is applied to the $\text{TM}_{80}\text{B}_{20}$ metallic glasses, the effective charge transfer (q) per B atom is 2.3, 1.6, and 1.4 for the alloys of Fe, Co, and Ni, respectively. For $\text{TM}_{80}\text{P}_{20}$, the deduced q values are 2.8, 2.7, and 2.4 (3). There is a qualitative consistency in these values in going from B (valency of 3) to P (valency of 5).

In the ternary systems, $\text{Fe}_{100-y} \text{M}_y \text{M}'_x$, where $\text{M} = \text{B}$ is partially replaced by $\text{M}' = \text{C}, \text{Si}, \text{Ge}$ or P , both C (valency of 4) and P were shown to cause decreases in the Fe moment, with P again being more effective (4). Although Si and Ge belong to the same column in the Periodic Table as C, they tend to increase the Fe moment, with Ge being more influential than Si (5). The charge transfer model thus lacks a quantitative basis in the sense that the q value has been shown to vary with the species of the metalloid as well as with the species of TM. Moreover, the model is incapable of predicting the q value to any degree of reliability.

We have initiated a study to further test the charge transfer model and to see whether or not the model is applicable to the alloy system in which the glass-forming metalloid is substituted by a metal, not another metalloid. Specifically, we chose $\text{Fe}_{82}\text{B}_{18}$ as the starting material from which a series of ternary alloys were derived of the compositions $\text{Fe}_{82}\text{B}_{18-x}\text{Be}_x$, where $x = 2, 4, 5,$ and 6 . Beryllium was selected as the second glass former to partially substitute for B because it is a typical metal with a well-defined valency of two.

The amorphous ternary system $\text{Fe}_{82}\text{B}_{18-x}\text{Be}_x$ displayed some interesting magnetic properties. The M_s at 4.2K and the deduced value for $\bar{\mu}_{\text{Fe}}$ first

showed an increase with x up to four, followed by a steady decrease, implying a peak between 4 and 5 at.% Be. The reversal of the M_s and $\bar{\mu}_{Fe}$ values was unexpected and difficult to understand because all of the alloys were single-phase solid solutions. The reversal seemed to imply a drastic change in the electronic structure of the system between $x=4$ and 5. We, therefore, resorted to using Auger electron spectroscopy as a new probe of the electronic structure of the amorphous Fe-B-Be alloys and to confirm this puzzling magnetic behavior.

It has been known (6) for some time that there are two basic types of Auger transitions depending on the interaction strength of the final two holes created by the Auger relaxation of the initial core hole. If the hole-hole interaction is strong, the Auger spectrum for a given Auger transition is derived from L-S type states formed by the two interacting holes. As a result, the local electronic environment of the atom is not reflected in the Auger lineshape. These quasiautomatic transitions occur whenever the XY holes are highly localized such as core level holes of the type KLL for $z > 10$. If the hole-hole interaction is weak, then the Auger lineshape of the XVV transition represents the self fold of the valence band density of states of the essentially independent final holes. The width of the Auger spectrum is approximately twice that of the occupied valence band, while the intensity is modulated by matrix-element effects across the band. These band-like spectra are sensitive probes of the local density of states (LDOS), and large lineshape changes are observed when such an element is placed into a different chemical environment. The delocalization essential to a weak hole-hole interaction is commonly found for sp type elements such as aluminum or magnesium rather than for

transition metals.

The metalloids (B, P, Si) which serve as glass formers are precisely those that form sp valence bands in their elemental solids. Therefore, they, and also Be, should exhibit band-like Auger spectra. When the initial core hole is created in a glass-forming atom, the XVV Auger spectrum should be a sensitive probe of the LDOS of these elements in metallic glasses. In particular, the effect of charge transfer from atoms of the glass-forming elements on the magnetic and electronic properties of the alloys can be directly studied as a function of composition and temperature.

Since metallic glasses are in a metastable state, irreversible transformation into the stable crystalline state should occur upon heating above the crystallization temperature. The crystallization processes are dependent on both temperature and time. The study of crystallization behavior of metallic glasses not only provides information on thermal stability of the glasses but also gives some insight into the nature of metallic glasses. Mössbauer spectroscopy has been successfully used to study crystallization processes and their products (7, 8). From those studies, interesting results about the structure and thermal stability of amorphous materials have been obtained. Therefore, Mössbauer spectroscopy was one of the experimental methods we used to supplement our magnetic characterization study and to furnish information on the crystallization behavior of the Fe-B-Be alloys.

B. Fe-B-Au

We also considered the effect of using a noble, monovalent metal, namely Au, to partially replace B, similar to our use of Be in the Fe-B-Be metallic glasses. According to the charge transfer model (3, 4), Au with its lower number of valence electrons (1 versus 3 for B) and its larger atomic radius (1.79Å versus 1.17Å for B) should cause the average Fe moment to increase over that of the Fe-B alloy. In addition, Felsch (9) has shown that in the binary amorphous Fe-Au films, the moment of the Fe increases with increasing Au content, reaching a maximum of $2.9 \mu_B$ -- a value previously observed from neutron data on Fe-Co (10). In crystalline Fe the fcc structure with a relatively large volume per unit cell is thought to have a moment of $2.8 \mu_B$ (11, 12), which may be related to the large lattice spacing of 3.64Å. In the Fe-Au films, the larger Au atoms leads to a larger lattice spacing, giving rise to a higher moment on the Fe atoms (13).

However, all the Fe-Au films of Felsch (9) crystallized below 295K and an exploitation of the high moment of the amorphous state is not possible in a useful temperature range. Therefore, another object of our study was to produce stable amorphous Fe-B-Au alloys with crystallization temperatures well above 300K. Our first attempt here was to prepare truly amorphous ribbons of Fe-B-Au alloys. Should our effort succeed, we would be able to test the validity of the beneficial effect of Au on the Fe moment; and also we could evaluate the charge transfer model by observing the effect of partially replacing B by Au in Fe-B.

C. Structural Study

In crystalline materials, sufficient information about the structure can be provided from the Bragg peaks obtained in an X-ray diffraction experiment. For amorphous materials, the absence of distinct structural periodicity results in the absence of Bragg peaks. However, the lack of periodicity does not preclude the existence of characteristic atomic arrangements with preferential bonding. A radial distribution function (RDF) of the broad diffraction peaks which result from short range order or bonding permits statistical characterization (averaged over the sample) in terms of the distances between an atom of a particular species and its nearest neighbors. The positions of the maxima in the RDF furnish the interatomic distance with the highest probabilities and the normalized areas under these maxima give an indication of the average number of nearest neighbors at the various mean distances. However, obtaining reliable information on the coordination number requires precise knowledge of the density of the specimen and the removal of data reduction artifacts caused by the termination of the X-ray scattering at finite values of $k=4\pi\sin\theta/\lambda$ where 2θ is the scattering angle and λ is the wavelength of the incident radiation. In some materials, there is still some structure sensitive information at the truncated value of k . There is great scientific interest in the structural information on metallic glasses because of the pronounced variation of certain physical and magnetic properties with a change in the type of metalloid and a change in the composition of the alloys. In this study, we were interested in obtaining structural information on $\text{Fe}_{82}\text{B}_{12}\text{C}_6$, $\text{Fe}_{82}\text{B}_{12}\text{Si}_6$, $\text{Fe}_{82}\text{B}_{14}\text{Be}_4$ and $\text{Fe}_{82}\text{B}_{13}\text{Be}_5$. The ternary alloys with C or Si were chosen because they have

been considered prime candidates for replacing crystalline Fe-Si sheets now used in power transformers, and a basic understanding of their properties is needed. Obtaining structural information on the Be alloys is a natural extension of our magnetic studies of the $\text{Fe}_{82}\text{B}_{18-x}\text{Be}_x$ metallic glasses from which, together with Auger electron spectroscopy, we detected a discrete change in the charge transfer behavior when the Be content is increased from 4 to 5 at.%. $\text{Fe}_{87}\text{B}_{13}$ was included in the latter study as a standard since RDF data are available on this alloy (14) and other Fe-B alloys near that composition (15, 16).

II. EXPERIMENTAL PROCEDURE

Because Be has the tendency to oxidation at high temperatures and also its toxicity requires special handling facilities, the five alloys were prepared in the following manner. First, a binary alloy was prepared by melting Fe and B, both of $\sim 99.9\%$ purity, inside an alumina crucible under high-purity helium atmosphere. The resulting alloy having a melting point around 1300°C was then remelted under similar conditions with Be of various amounts to meet the nominal compositions. Each alloy was held at 1100°C for 18 hours to attain composition homogeneity, and weight loss was checked at each step to assure that the composition was maintained. Amorphous ribbons were prepared by quenching the melt onto a 23 cm copper wheel rotating at 3700 rpm. Ribbons thus produced were 1-2 mm wide, ~ 0.02 mm thick, and of varying lengths up to 30 meters. Brittle ribbons were rejected, and to further ascertain the noncrystallinity of the ductile ribbons we relied on the X-ray examination, using either a diffractometer or a powder camera. Magnetizations of the ribbons were measured in a vibrating-sample magnetometer under a magnetic field of up to 20 kOe in the temperature range 4.2-1000K. The annealing behavior of the amorphous ribbons was studied by monitoring the magnetization (M) under a constant field of 50 Oe while the temperature was rising at a rate of about 2° per minute. Comparison of previous (17) and our results indicated that the low-field responses were more sensitive to the onset of magnetic and crystallization transitions than saturating fields above 7.5 kOe. The low-field M vs. T spectra allow the Curie (T_C) and two crystallization (T_{x1} and T_{x2}) temperatures to be determined. T_C

is obtained by extrapolating to $M=0$ the first descending portion of the M vs. T curve, while T_{x1} and T_{x2} are taken as the temperatures where M shows a change in slope in the segment after passing T_C .

For the identification of the crystalline phases, ribbons containing 4 and 6 at.% Be were sealed in quartz tubes under a residual pressure of 6×10^{-7} torr and annealed for two hours slightly above T_{x1} or T_{x2} . The annealed ribbons were examined by the X-ray powder method.

Wet chemical analyses on the ribbons gave results on the Be content which are compared with the nominal values in Table 1. Serious discrepancies exist for the first two ternary alloys. The report that Be was nondetectable in the $Fe_{82}B_{16}Be_2$ ribbon was particularly disturbing because analysis by Auger electron spectroscopy (AES) together with ion bombardment clearly showed the presence of Be in the bulk of the ribbons.

In the AES experiments, random sections of each alloy in ribbon form about 1 cm long and 0.1-0.2 cm wide, were mounted in the Auger spectrometer which consisted of a Physical Electronics Model 10-155 cylindrical mirror analyzer with a coaxial 5 keV electron gun. The analyzer has an energy resolution of 0.6%. The electron beam had 3 keV energy, a beam current of 2.0 μA and a spot size of approximately 100 microns. Intensive Ar^+ ion bombardment at 3 keV with a current density near 100 $\mu A/cm^2$ was required to prevent reabsorption of carbon- and oxygen-bearing gases onto the sample surface; otherwise carbon and oxygen strongly affect the Auger lineshape of the B and Be atoms. The Auger spectra reported here were taken only after the O(510 eV) and C(272 eV) peaks had disappeared into the noise level. From their relative sensitivity factors (18), the surface concentration of either element was estimated to be less than 0.1

Table 1. Magnetization (M_S) at 18 kOe and 4.2K, Fe moment ($\bar{\mu}_{Fe}$), Curie (T_C) and two crystallization temperatures of $Fe_{82}B_{18-x}Be_x$ alloys

Alloy	% Be by weight		M_S , emu/g	$\bar{\mu}_{Fe}$, μ_B	T_C , °C	T_{x1} , °C	T_{x2} , °C
	nominal	analyzed ^a					
$Fe_{82}B_{18}$	0	0	190 \pm 1	1.98 \pm .01	371 \pm 2	400 \pm 3	not observed
$Fe_{82}B_{16}Be_2$	0.38	not detected	198 \pm 2	2.14 \pm .04	339 \pm 2	416 \pm 5	471 \pm 2
$Fe_{82}B_{14}Be_4$	0.76	0.071	200 \pm 2	2.21 \pm .05	313 \pm 5	397 \pm 2	466 \pm 5
$Fe_{82}B_{13}Be_5$	0.95	0.77	194 \pm 1	2.04 \pm .01		not available	
$Fe_{82}B_{12}Be_6$	1.14	1.10	189 \pm 2	2.02 \pm .03	303 \pm 2	390 \pm 5	458 \pm 5

^aSubject to $\pm 10\%$ uncertainty.

at.%, which was insufficient to affect the KVV spectra of B or Be.

For the Mössbauer experiments, the glassy, as-quenched ribbons 2 mm wide, 15 mm long and approximately 0.02 mm thick, were placed parallel to each other and attached to a plastic substrate by vacuum grease and used as absorbers. In the annealing experiments, ribbons were sealed into a quartz tube and after evacuating down to 2×10^{-7} torr were placed in a pre-heated furnace at annealing temperatures indicated below for 2-3 hours. For low temperature measurements the ribbons were held in place on a beryllium disk by vacuum grease and clamped onto a copper rod which was connected to the liquid nitrogen reservoir in a stainless steel cryostat with a beryllium window.

The Mössbauer spectra were obtained with a Ranger Electronics spectrometer coupled with a TMC 1024 channel analyzer operated in both constant acceleration and Region of Interest (ROI) modes. An Armco iron foil was used in velocity calibration. A typical iron spectrum has an inner line width of 0.25 mm/sec and an isomer shift of -0.214 mm/sec relative to the source at room temperature. The source is 11.5 mCi ^{57}Co in copper matrix with a line width of 0.107 mm/sec. All the spectra taken throughout the experiments contained approximately $(150-450) \times 10^3$ counts per channel in each 1024-channel spectrum.

Ingots of the Fe-B-Au alloys were prepared by induction melting of the constituents under argon atmosphere in a quartz crucible. The alloys were quenched onto the surface of a copper wheel moving with a linear speed of 55 m/sec. Ribbons of 0.02 mm thick and about 1 mm wide were obtained. The addition of Au to Fe-B made the ternary alloys very difficult to be quenched into amorphous ribbons. Although continuous

ribbons could be obtained by using a low surface speed (less than 30 m/sec), the resulting ribbons were not amorphous. Linear speeds of around 55 m/sec caused the ribbons to be very thin and thus provided the high quenching rate needed to obtain amorphous ribbons. As the Au content was increased, the wheel speed had to be increased and higher melt temperatures were needed. The resulting lower viscosity of the melt made it easier for the melt to flow on the wheel surface and provide continuous ribbons. When the Au content was increased to over 2 at.%, no completely amorphous ribbons were obtained.

The chemical compositions of the ribbons were determined by wet chemistry and by electron microprobe methods and the results are listed in Table 2. The microprobe analysis indicates a composition close to the nominal in all cases, but the wet chemical analysis indicate lower Au content than the nominal in the one alloy designated as $\text{Fe}_{82}\text{B}_{17}\text{Au}_{1.0}$. The magnetization of the as-quenched ribbons was measured at 4.2K in a vibrating sample magnetometer (VSM). Thermomagnetic scans (M vs. T) of these alloys were taken in the VSM in the temperature range of 295 to 1010K with a heating rate of 10K/min below 600K and 2K/min beyond that temperature.

Similar thermomagnetic scans were taken of another alloy of analyzed composition, $\text{Fe}_{87}\text{B}_{11}\text{Au}_2$. Ribbons of that alloy were also sealed in quartz capsules with a residual pressure of 2×10^{-7} torr. The ribbons were annealed at 568K, 678K, 708K, 758K, 793K, and 884K for 25 minutes by introducing each capsule into a copper block maintained at the annealing temperature. The temperature reported above are the average temperatures for the last 15 minutes of annealing, during which time less than 1K variation was observed. The thermocouple was also attached to the copper

Table 2. Comparison of nominal and analyzed compositions of Fe-B-Au alloys

Alloy	Nominal Au weight %	Analyzed Au weight %	
		by wet chemical analysis ^a	by electron microprobe analysis ^a
Fe ₈₂ B _{17.5} Au _{0.5}	2.62	2.87	2.7
Fe ₈₂ B ₁₇ Au _{1.0}	3.97	2.80	4.5
Fe ₈₂ B _{16.5} Au _{1.5}	5.85	5.86	6.9

^aThe results are subject to +10% uncertainty.

block. The block and the capsule were removed from the furnace and air-cooled. The magnetization of these annealed ribbons was also measured at 4.2K in the VSM. The crystalline phases of the ribbons were determined by X-ray diffraction by the Debye-Scherrer method and with a diffractometer using a step-scan method with 0.04 degree steps with either a constant intensity count of 2000 or a 60 second time constant.

The Fe-B-Be specimens used in the RDF experiments were sections of the same ribbons on which the magnetization measurements were conducted. The $\text{Fe}_{87}\text{B}_{13}$, $\text{Fe}_{82}\text{B}_{12}\text{Si}_6$, and $\text{Fe}_{82}\text{B}_{12}\text{C}_6$ were prepared in ribbon form using the same equipment. A short section of each ribbon was mounted on a goniometer with both the long axis and the large lateral axis initially normal to the incident X-ray beam. The intensities were measured in a transmission mode with a θ - 2θ scan. The X-ray source was a standard focus molybdenum target tube operated at 60KV and 25mA. The scattered MoK_α radiation was selected with a graphite monochromator using the (002) planes and a 2α value of 12.2° . The detection system consisted of a scintillation counter, linear amplifier, pulse height analyzer, and a scaler-timer. The data collection system was under computer control.

Diffacted intensities were measured at room temperature from $2\theta=3.0^\circ$ to 96° at a $\Delta 2\theta$ interval of 0.20° (from $k=0.5$ to 12.9\AA^{-1} , $\lambda=0.7107\text{\AA}$). The intensities were obtained in the form of time needed for a fixed number of counts (2000 for the specimens, 500 for background, i.e., without a specimen present) to reach the detector. This method helped to keep the statistics uniform over the angular range. The time varied from 60 seconds to over 1200 seconds per data point. Long term instrumental drift and varying air scatter problems for these long

counting times are to be expected, but these problems may be minimized by accumulating and averaging data over several scans. However, the data used in this experiment came from one scan and in the analyses $k_{\max} = 10.0\text{\AA}^{-1}$ was used instead of $k_{\max} = 12.9\text{\AA}^{-1}$ since we observed a spurious rise of the intensity from some specimens beyond $k = 10.0\text{\AA}^{-1}$.

III. DATA REDUCTION METHOD FOR RADIAL DISTRIBUTION FUNCTIONS

The radial distribution function (RDF) is calculated from the structure sensitive part of the coherent X-ray scattering from a specimen using the Fourier integral (19):

$$\text{RDF} = 4\pi r^2 \rho(r) = 4\pi r^2 \rho_0 + (2r/\pi) \int_0^\infty k [S(k)-1] \sin(kr) dk \quad (1)$$

where $S(k)$ is called the total interference function or structure factor; r is the distance in angstroms from any arbitrary atom taken as the origin; ρ_0 is the average scattering density of the specimen and is proportional to the bulk density and $k = 4\pi \sin\theta/\lambda$, as defined previously.

To obtain the structure sensitive intensity from the scattered X-ray intensity, several of the usual corrections have to be made. The data are corrected for background and then for absorption in the transmission geometry used. The absorption correction is of the form

$$I_{0^\circ}/I_{2\theta} = \mu t(1-\sec 2\theta)/\{\exp[\mu t(1-\sec 2\theta)] - 1\} \quad (2)$$

where μ is the absorption coefficient and t is the thickness of the sample. The polarization correction is of the form

$$P = (\cos^2 2\alpha + \cos^2 2\theta)/(1 + \cos^2 2\alpha) \quad (3)$$

where 2α is the monochromator angle ($2\alpha=12.2^\circ$ for (002) planes of graphite). No correction was made for multiple scattering. The intensity data now contain both structure sensitive and independent coherent scattering and the incoherent (Compton) scattering. The amount of Compton correction needed is a bit elusive and cannot experimentally be determined precisely.

A multiplier of the Compton correction (called a discrimination function varying from 0 to 1) is determined by assuming that at high values of 2θ there is almost no structure sensitive scattering and the observed scattering is made up of independent coherent and Compton scattering. Hence, the experimental data can be normalized to the theoretical scattering and the data should oscillate about the value of 1 and decay to 1. To enforce this requirement, the discrimination function of the Compton is adjusted. However, the greater the degree of atomic order in the specimen, the greater k_{\max} must be in order for the above assumption to be valid, and normalization errors can be made when one tries to enforce this requirement. Metallic glasses tend to have structure sensitive coherent scattering at quite large k values. Therefore, in this work, normalization was done both at high k values and by the integral RDF method with a sharpening function of the gaussian form, $e^{-.008k^2}$, which had the effect of minimizing any dependent coherent scattering at high k and making the assumption applicable.

The experimental coherent scattering is adjusted by subtracting the independent coherent scattering in the following manner:

$$\text{Structure factor} \equiv S(k) = [(I_{\text{coh}}(k) - \langle f^2 \rangle + \langle f \rangle^2) / \langle f \rangle^2] \quad (4)$$

where $\langle f^2 \rangle = \sum c_j f_j^2$, $\langle f \rangle = \sum c_j f_j$ with f_j = atomic scattering factor adjusted for anomalous scattering ($f_j = f_j^0 + \Delta f_j^1 + i\Delta f_j''$) and c_j = atomic concentration of the j th atom.

The expression $4\pi r^2 \rho(r) dr$ gives the number of atoms in a spherical shell of thickness dr and radius r about any arbitrary origin atom. A numerical integration of Eq. (1) yields $4\pi r^2 \rho(r)$ and the areas under the

peaks in the RDF curve give the number of atoms related to these peaks. It should be immediately apparent that careful and consistent scaling of the data to the theoretical scattering is needed to obtain reliable information on the number of atoms. However, reliable information can still be obtained about the peak position from the reduced RDF integral

$$G(r) = 4\pi r [\rho(r) - \rho_0] = 2/\pi \int_0^\infty k [S(k)-1] \sin(kr) dk \quad (5)$$

since $G(r)$ requires no knowledge of ρ_0 and is not as sensitively dependent on the normalization factor as in the RDF in Eq. (1).

The limits of the integrals in Eq. (1) and (5) are $k=0$ and ∞ . The function $k[S(k)-1] \equiv F(k)$ is limited to k_{\max} and hence the integral has to be truncated which introduces a step function. In the Fourier integral theorem, a step function will transform as oscillations with period, $\Delta r = 2\pi/k_{\max}$ in the transformed space (r space). Therefore, it is important that $F(k)$ be very close to zero at the upper limit of the integral. Since there are perceptible deviations from zero in $F(k)$ at the k_{\max} usually encountered, an artificial temperature factor (a damping factor) is introduced to smooth out these oscillations. The effect of the factor is to reduce the contribution of $F(k)$ at high k values to the final integral, thus minimizing the amplitude of ripples caused by the finite termination of the integral limit and the amplitude of those caused by any spurious peaks at large k with period of $\Delta r = 2\pi/k_{\text{peak}}$. The integral now becomes:

$$G(r) = 2/\pi \int_0^{k_{\max}} F(k) e^{-Bk^2} \sin(kr) dk \quad (6)$$

where B is chosen so that at k_{\max} , $e^{-Bk^2} = 0.1$. The temperature factor

can also cause broadening in the peaks and may obscure small shoulders on the peaks, however.

Another consequence of a finite limit of the integral in $G(r)$ is the effective introduction of a window function (20), $M(k)$

$$\text{where } \begin{aligned} M(k) &= 1 & 0 \leq k \leq k_{\max} \\ M(k) &= 0 & k > k_{\max} \end{aligned}$$

$G(r)$ is effectively convolution broadened by the function $m(r)$ which is a cosine Fourier Transform of $M(k)$

$$m(r) = 1/\pi \int M(k) \cos(kr) dk = \frac{k_{\max}/\pi [\sin(k_{\max} r)]}{k_{\max} r} \quad (7)$$

For $k_{\max} = 10.0 \text{ \AA}^{-1}$, the broadening of the peak width at half-maximum is $3.8/k_{\max} = 0.38 \text{ \AA}$ which makes separation of the first peak in $G(r)$ into two or three peaks very difficult in binary metallic glasses when the size difference $(r_1 - r_2)/r_1 < 30\%$.

The integral $G(r)$ in the work was evaluated with $k_{\max} = 10.0 \text{ \AA}^{-1}$ and with a Δr interval of 0.05 up to $r_{\max} = 15$. An evaluation with $\Delta r = 0.02$ did not significantly improve the resolution of the peaks. The $G(r)$ curves contained the expected oscillations at $r < 2 \text{ \AA}$. It is expected that

$$[dG(r)/dr]_{r=0} = -4\pi\rho_0$$

and $G(r)$ should be a straight line for r values less than the diameter of the smallest atom. Therefore, the oscillations are obviously spurious and are artifacts of the Fourier transformation process resulting from a finite k_{\max} termination of $F(k)$. This was confirmed by varying B in Eq. (6) until the oscillations disappeared, or by a process of removing those oscillations at $r < 2 \text{ \AA}$ and Fourier transforming $G(r)$ to obtain $F(k)$ and

comparing this $F_{\text{coh}}(k)$ to the experimental $F_{\text{exp}}(k)$. Obtaining the profile of $F_{\text{exp}}(k)$ is taken as a good indication of the spurious origin of the oscillations at $r < 2\text{\AA}$. This method first introduced by Kaplow et al. (21) has been widely used. It also has the benefit of improving the erroneous normalization of experimental data. Wagner (20) recommends against using this procedure since it removes only the oscillations at small values of r . Instead, he suggests varying $F(k)$ in a self-consistent manner, through the discrimination function of the Compton scattering. However, the main peak positions in $G(r)$ are unaffected by the specific procedure used because any oscillations at higher r values are within the noise level.

The number of nearest neighbors was calculated from the area under the first maximum (minimum to minimum) in the complete RDF curve. This curve was calculated from

$$\text{RDF} \equiv 4\pi r^2 \rho = rG(r) + 4\pi r^2 \rho_0 \quad (8)$$

where the ρ_0 values used are experimental values from published data.

IV. RESULTS AND DISCUSSION

A. Fe-B-Be

1. Magnetic and thermomagnetic behavior

As might be expected, the amorphous ribbons of all five alloys displayed little magnetic anisotropy. Hence the ribbons readily attained M_s at moderate applied fields below 10 kOe. The M_s values obtained in emu/g at 18 kOe and 4.2K are listed in Table 1. A trend is seen in that the substitution of Be for B led first to an increase in M_s from 190 emu/g for $\text{Fe}_{82}\text{B}_{18}$ to a maximum of 200 emu/g for $\text{Fe}_{82}\text{B}_{14}\text{Be}_4$, then to a steady decrease when the Be content exceeded 4 at.%. Using the analyzed compositions to calculate the atomic weight of each alloy and assuming that only the iron atoms carry moments, the emu/g values are converted into average Bohr magneton numbers per iron atom ($\bar{\mu}_{\text{Fe}}$). The deduced $\bar{\mu}_{\text{Fe}}$ values shown in Table 1 reveal the same trend despite the composition uncertainty in the first two ternary alloys. Note that the maximum $\bar{\mu}_{\text{Fe}}$ value of $2.2\mu_B$ for the 4 at.% Be alloy is about the same as the atomic moment in the crystalline iron (22) and is higher than $\bar{\mu}_{\text{Fe}} = 2.0\mu_B$ extrapolated for the "amorphous" iron at 4.2K (23). These comparisons signify the benefit of the initial substitution of Be for B in the amorphous Fe-B alloys.

The measured T_C of the amorphous alloys are listed in Table 1. The effect of Be on T_C is seen to be monotonically decreasing. The T_C drop from 371°C for $\text{Fe}_{82}\text{B}_{18}$ to 303°C for $\text{Fe}_{82}\text{B}_{12}\text{Be}_6$ amounts to a nontrivial 10.6%. Also worth noting are the different trends in which M_s or $\bar{\mu}_{\text{Fe}}$ and T_C vary with the Be content.

The changes in the magnetic response (M) with temperature at $H = 50$

0e are shown for the ribbons containing 2, 4, and 6 at.% Be in Figure 1. The experimental data on T_{x1} and T_{x2} for the alloys are listed in Table 1. Our M vs. T curve for the binary $\text{Fe}_{82}\text{B}_{18}$ (not shown) agrees qualitatively with previous work (17) in that this alloy displayed only one crystallization stage. For the ternary alloys, at least two crystallization stages were observed. Also, it appears that Be has the effect of widening the paramagnetic region between T_C and T_{x1} , but this may result from a lowering of T_C and not from any appreciable increase in T_{x1} . The X-ray results of the annealing experiments on $\text{Fe}_{82}\text{B}_{18-x}\text{Be}_x$ indicate that at $T \geq T_{x1}$, the ribbons crystallize to produce an α -Fe phase. Annealing the ribbons at $T \geq T_{y2}$ yielded another phase which was identified as Fe_2B . Using the reported lattice parameter (a_0) data for crystalline Fe-Be solid solutions (24), the values of a_0 deduced from the d spacings listed in Table 3 imply the presence of Be in the α -Fe phase.

Two aspects of the magnetic behavior of the present amorphous alloys are considered unusual in comparison with the $\text{Fe}_{100-x}(\text{M}, \text{M}')_x$ alloys. First, the effect of Be on M_S and $\bar{\mu}_{\text{Fe}}$ in the present alloys is not monotonically increasing or decreasing as was the case with M' in the latter alloys (5). Certainly, the reversal from an initial increase to a decrease in M_S and $\bar{\mu}_{\text{Fe}}$ beyond 4 at.% Be has not been observed in the Fe-metalloid alloys. Second, the change (increase or decrease) in T_C has always been parallel to the change in $\bar{\mu}_{\text{Fe}}$ in the Fe-(M, M') alloys, but such parallelism did not appear in the present alloys. Instead, their T_C values show a monotonic decrease with the Be content. While the initial increase in M_S and $\bar{\mu}_{\text{Fe}}$ may be ascribed to the lower charge transfer of Be by virtue of its divalency as against trivalency of B, the subsequent

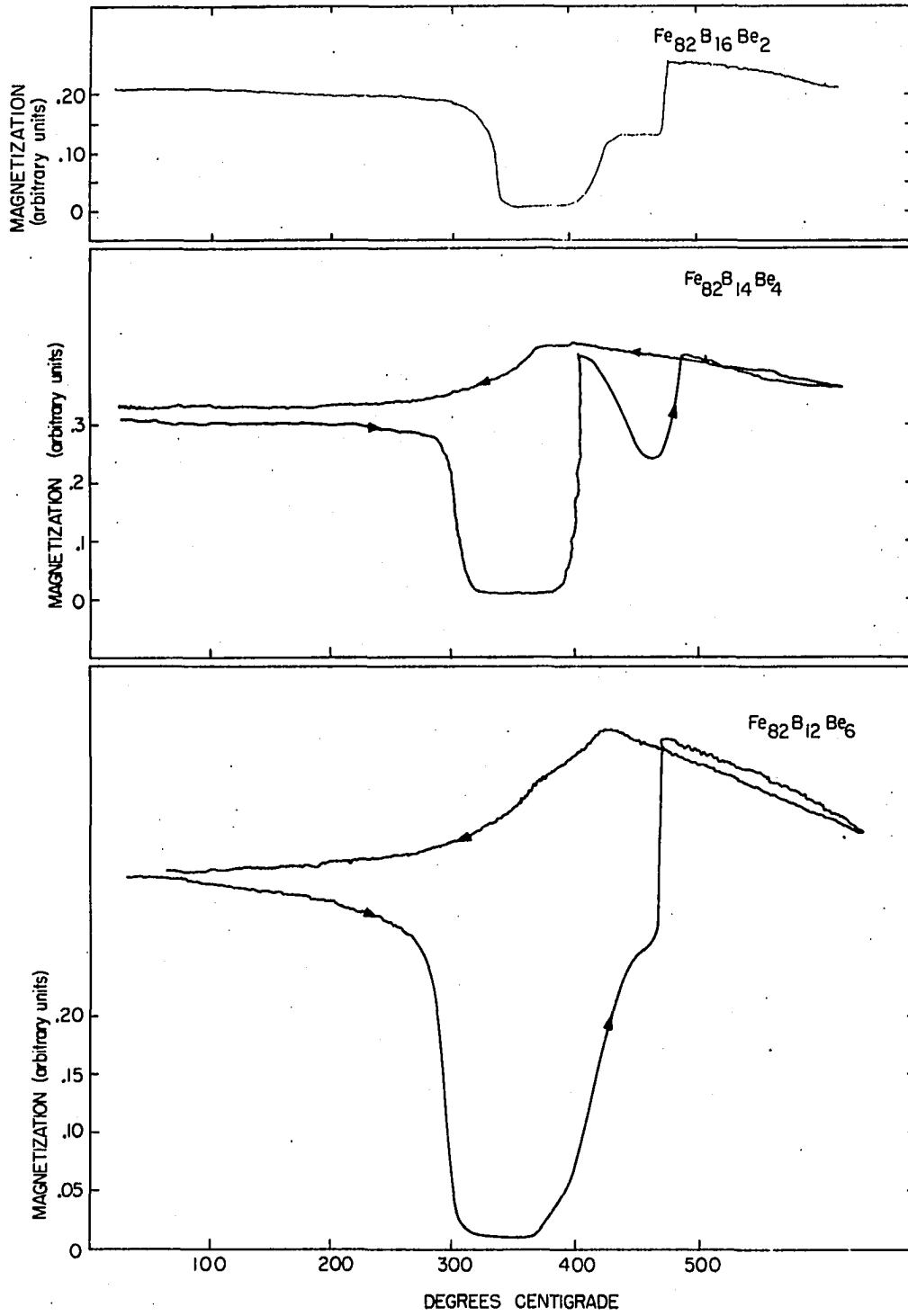


Figure 1. Thermomagnetic data showing the annealing behavior of three amorphous $\text{Fe}_{82}\text{B}_{18-x}\text{Be}_x$ alloys

Table 3. Annealing temperatures, d-spacings, crystallographic indices, hkl, and annealing products of Fe-Be-Be alloys

Alloy	693K			758K			793K		
	d	hkl	phase	d	hkl	phase	d	hkl	phase
Fe ₈₂ B ₁₆ Be ₂	2.0251	110 β	α -Fe(Be)				3.6320	110	Fe ₂ B
	2.0267	110	α -Fe(Be)				2.0301	110 β	α -Fe(Be)
	1.4340	200	α -Fe(Be)				2.1068	002	Fe ₂ B
	1.0107	220	α -Fe(Be)				2.0323	110	α -Fe(Be)
	1.1654	211	α -Fe(Be)				1.6311	202	Fe ₂ B
							1.4366	200	α -Fe(Be)
							1.1671	211	α -Fe(Be)
							1.0124	220 α_1	α -Fe(Be)
							1.0125	220 α_2	α -Fe(Be)
							0.9060	310 α_1	α -Fe(Be)
						0.9058	310 α_2	α -Fe(Be)	
Fe ₈₂ B ₁₄ Be ₄	2.0333	110 β	α -Fe(Be)						
	2.0328	110	α -Fe(Be)	2.0277	110	α -Fe(Be)	3.6329	110	Fe ₂ B
	1.4379	200	α -Fe(Be)	1.6309	202	Fe ₂ B	2.0323	110	α -Fe(Be)
	1.0119	220 α_1	α -Fe(Be)	1.4319	200	α -Fe(Be)	2.1101	002	Fe ₂ B
	1.0116	220 α_2	α -Fe(Be)	1.1988			2.0328	110	α -Fe(Be)
	1.1651	211 α_1	α -Fe(Be)	1.1713	211	α -Fe(Be)	1.6271	202	Fe ₂ B
	1.1652	211 α_2	α -Fe(Be)	1.0148	220	α -Fe(Be)	1.4375	200	α -Fe(Be)
				0.9071	310	α -Fe(Be)	1.1659	211	α -Fe(Be)
				0.8243	222	α -Fe(Be)	1.0124	220 α_1	α -Fe(Be)
				0.7677	321	α -Fe(Be)	1.0125	220 α_2	α -Fe(Be)
							0.9061	310 α_1	α -Fe(Be)
							0.9060	310 α_2	α -Fe(Be)

Table 3. (Continued)

Alloy	693K			758K			793K		
	d	hkl	phase	d	hkl	phase	d	hkl	phase
$\text{Fe}_{82}\text{B}_{13}\text{Be}_5$	2.0244	110 β	α -Fe(Be)				3.6698	110	Fe ₂ B
	2.0274	110	α -Fe(Be)				2.5861	200	Fe ₂ B
	1.1637	211	α -Fe(Be)				2.0323	110 β	α -Fe(Be)
	1.0107	220	α -Fe(Be)				2.1210	002	Fe ₂ B
							2.0335	110	α -Fe(Be)
							1.9450		
							1.6408	202	Fe ₂ B
							1.4360	200	α -Fe(Be)
							1.1676	211	α -Fe(Be)
							1.0130	220 α_1	α -Fe(Be)
							1.0129	220 α_2	α -Fe(Be)
							0.9064	310 α_1	α -Fe(Be)
							0.9062	310 α_2	α -Fe(Be)
$\text{Fe}_{82}\text{B}_{12}\text{Be}_6$	2.0301	110 β	α -Fe(Be)	3.6775	110	Fe ₂ B			
	2.0287	110	α -Fe(Be)	2.0282	110	α -Fe(Be)			
	1.4322	200	α -Fe(Be)	2.1232	002	Fe ₂ B			
	1.1661	211	α -Fe(Be)	2.0272	110	α -Fe(Be)			
	1.0406	220	α -Fe(Be)	1.6435	202	Fe ₂ B			
	0.9044	310	α -Fe(Be)	1.1669	211	α -Fe(Be)			
				1.0107	220 α_1	α -Fe(Be)			
				1.0111	220 α_2	α -Fe(Be)			
				0.9047	310 α_1	α -Fe(Be)			
				0.9048	310 α_2	α -Fe(Be)			

decrease in M_s and $\bar{\mu}_{Fe}$ is difficult to understand unless the higher contents of Be led to the formation of a second phase, which was not so strongly ferromagnetic. This possibility was quickly ruled out, however, because reexamination of the X-ray powder patterns of the 5 and 6 at.% Be alloys showed no evidence of a second phase, either amorphous or crystalline. Subsequently, we resorted to other techniques and examined the ribbons of the binary and all four ternary alloys by Auger electron spectroscopy (AES) and Mössbauer spectroscopy (MS) at room temperature. Detailed descriptions of the new results are given below.

2. Auger electronic spectroscopy as a probe of the electronic structure

Figures 2 and 3 show the Auger spectrum of $Fe_{82}B_{14}Be_4$ and $Fe_{82}B_{13}Be_5$, respectively, in the energy range 75 to 200 eV under conditions of nearly identical spectrometer gain. These spectra were reproducible and representative of several measurements taken at various positions along the ribbon length. The Auger transition energies used in these figures were measured at the largest negative-going peaks of the spectra. The most significant result, evident from comparing Figures 2 and 3, is that the Be KVV transition for $x=4$ occurs at 92.3 eV but for $x=5$ it appears at 106.2 eV. Such a large energy shift of 13.9 eV for such a small change in composition is rare. Spectra taken (not shown) for $x=2$ show the Be KVV transition at the same lower energy as for $x=4$, while that for $x=6$ show the Be KVV transition at 106 eV, close to that for $x=5$. Therefore, we conclude that there is a large shift in the energy of the Be KVV transition between 4 and 5 at.% Be. No transition was observed near 106 eV (at the five percent level) for $x \leq 4$ and near 92 eV (at the ten percent

AUGER SPECTRUM

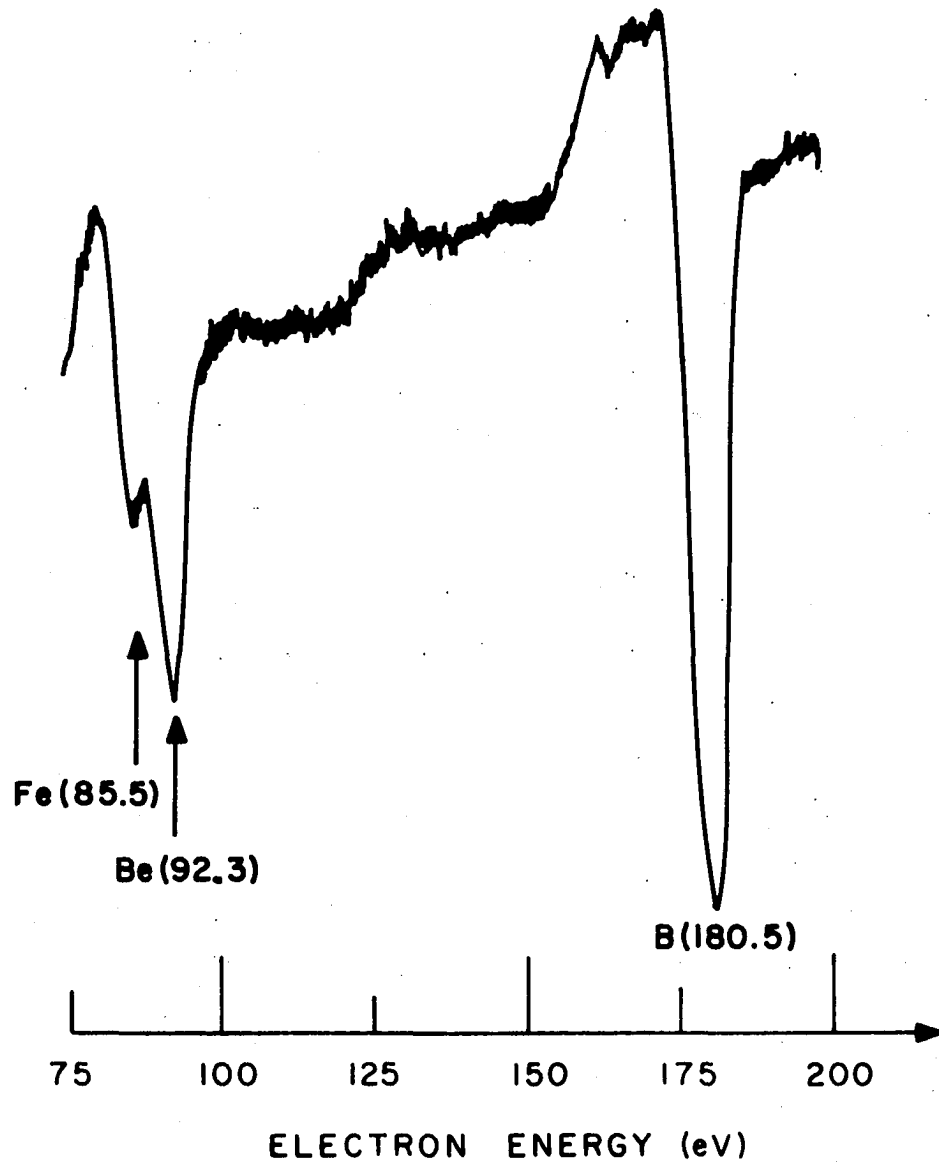
SPUTTER CLEANED amorphous- $\text{Fe}_{82}\text{B}_{14}\text{Be}_4$ 

Figure 2. Auger electron spectrum of sputter-cleaned amorphous $\text{Fe}_{82}\text{B}_{14}\text{Be}_4$ showing the Fe M_1VV transition at 85.5 eV, the Be KVV transition at 92.3 eV and the B KVV transition at 180.5 eV

AUGER SPECTRUM

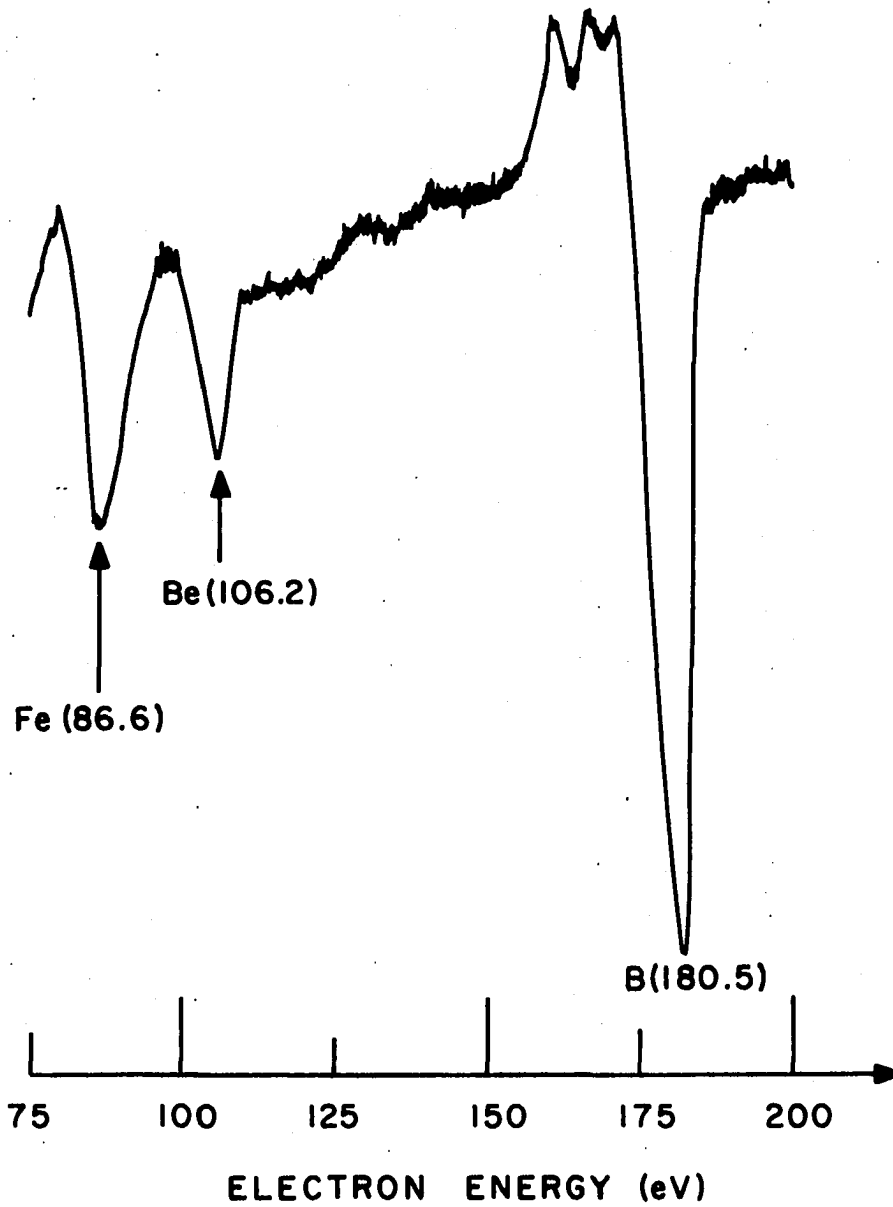
SPUTTER CLEANED amorphous- $\text{Fe}_{82}\text{B}_{13}\text{Be}_5$ 

Figure 3. Auger electron spectrum of sputter-cleaned amorphous $\text{Fe}_{82}\text{B}_{13}\text{Be}_5$. There is a large shift in the Be KVV transition from 92.3 eV shown in Figure 2 to 106.2 eV

level) for $x \geq 5$. In contrast to the Be KVV spectra, few changes were observed for the B KVV transition at 180 eV, nor for any of the Auger transitions of Fe.

The energy shift of the Be KVV transition correlates very well with the magnetic behavior of the amorphous alloys because the shift occurs between $x=4$ and 5 where M_s and $\bar{\mu}_{Fe}$ also display a reversal. Our application of AES has thus succeeded in reinforcing the revelation from the magnetic data that the $Fe_{82}B_{18-x}Be_x$ alloys undergo a drastic change in the electronic structure from $x=4$ to $x=5$.

Before discussing the implications of the Be KVV energy shift, it is instructive to recall that a similar shift has been observed between Be and BeO. The KVV Auger transition for the Be metal is a single asymmetric peak at 104 eV (25). This peak arises mainly from the K2p2p Auger transition, whereas the asymmetry comes about because of an initial state screening in the Be metal, which enhances the K2s2p transition on the low energy side (26). For BeO, a series of Auger lines were observed at and below 94 eV, which were attributed to interatomic transitions of the type $K0(2sp)0(2sp)$ (27). Because all of the Be valence electrons in the oxide have been transferred to the LDOS of oxygen, the final state holes originate in the 2sp LDOS of oxygen. The present observation of a shift in the Be KVV Auger spectrum from 106 to 92 eV in the $Fe_{82}B_{18-x}Be_x$ amorphous alloys can also be explained by assuming a charge transfer of the 2sp valence electrons from the LDOS of Be. In alloys with $x \leq 4$, the shift occurs much like the charge transfer envisioned for BeO, whereas in alloys with $x \geq 5$, the Be valence electrons are retained in the LDOS of Be similar to that of the Be metal. Since none of the amorphous alloys displayed

both the 106 and the 92 eV lines, the charge transfer for $x \leq 4$ must involve nearly all of the Be atoms. This implies that a complete change in the local environment of all of the Be atom sites occurs when x goes from 4 to 5.

After having established the removal of the 2sp electrons from the Be LDOS for $x \leq 4$, it is only natural to ask: "Where have the electrons gone?" There are three possibilities: (1) they could go to the LDOS of B, (2) they could appear in the LDOS of Fe, or (3) they could reside in the delocalized conduction band. Consider first the LDOS of boron. At $x=4$, which amounts to $\sim 29\%$ of the B concentration, and because there are two valence electrons to be transferred per Be atom, the increase in the electron concentration of the B LDOS would be appreciable. Such an increase plus the fact that the B KVV Auger spectrum is also band-like would produce an observable change in the LVV spectrum of B. Figures 2 and 3 show no changes in the lineshape for the B(180) Auger transition, however. Therefore, the first possibility is ruled out. Now if the Be valence electrons are transferred to Fe, the change in the Auger spectrum of Fe is expected to be much less than that for B. This is partly because the Fe Auger transitions are predominantly quasiatomic and partly because the concentration of Fe is 5-6 times higher than Be. Hence, any LDOS changes for Fe would be very difficult to observe in the Auger spectrum of Fe. Little or no change in the $M_{2,3}VV(48 \text{ eV})$, $M_1VV(86 \text{ eV})$, $L_3M_{2,3}M_{2,3}(600 \text{ eV})$, $L_3M_{2,3}M_{4,5}(650 \text{ eV})$, or the $L_3M_{4,5}M_{4,5}(700 \text{ eV})$ Fe Auger transitions was observed for any of the alloys investigated. Recently Jennison (28) has shown that the pd contribution to the M_1VV Auger line of copper is band-like. By analogy, the same transition in Fe should also be

band-like. Unfortunately, the energy range of the pd contribution to the weak Fe M_{7VV} line falls near the 92 eV peak of Be for $x \leq 4$, thereby making it impossible to detect any changes in the M_{7VV} line. This awkward situation has prevented us from deciding whether the LDOS of Fe or the conduction band density of states has been affected by the loss of the Be valence electrons for $x \leq 4$.

Despite the uncertainty on the whereabouts of the transferred 2sp electrons of Be, our Auger results have furnished significant information on the $Fe_{82}B_{18-x}Be_x$ metallic glasses in two aspects. First, a charge transfer of the type usually found only in ionic compounds has been established in metallic glasses. Second, the presence of this charge transfer for $x \leq 4$ and its absence for $x \geq 5$ correlate remarkably well with the reversal of the M_s and $\bar{\mu}_{Fe}$ values upon increasing x from 4 to 5. The Auger results have thus substantiated our previous conclusion drawn from magnetic data that fundamental changes occur in the electronic structure between $x=4$ and 5 in this system.

In this section, we have demonstrated that the analysis of the energies and lineshape of KVV Auger transition of glass-forming elements in metallic glasses offers a new, sensitive method for probing the LDOS of this class of materials. Auger analysis should prove more generally applicable than either Mössbauer spectroscopy or NMR spectroscopy, which are restricted to certain nuclei. The AES method suffers no such restriction because the TM-M metallic glasses always contain the sp elements with band-like KVV Auger spectra. The method also has a distinct advantage over the photoemission valence-band study, especially in the multi-component glasses of commercial interest. While the photoemission study

probes the total valence band density of states and not the contributions of individual elements, AES can separately determine the LDOS of each element by virtue of its requirement for an initial core hole. Hence, AES has the potential to isolate the effects of various elements in a particular system. We expect that Auger analysis of the KVV transitions will complement other techniques in the study of the electronic and magnetic properties of this large class of materials.

Note: The Auger electron spectroscopy work reported in this section was done in collaboration with A. J. Bevolo of the Solid State Physics Division of Ames Laboratory who performed the Auger experiments. Further details are reported in a journal article entitled, "Probing the Electronic Structure of Amorphous Alloys by Auger XVV Transition Glass-Forming Elements," by A. J. Bevolo, C. S. Severin, and C. W. Chen, submitted to Phys. Rev. Lett.

3. Mössbauer spectroscopy

a. Hyperfine-field distribution and isomer shift The Mössbauer spectra for the $\text{Fe}_{82}\text{B}_{18-x}\text{Be}_x$ alloy (Figure 4) are similar in appearance to those of other amorphous alloys having Fe as the only magnetic atom. The results of a distribution of isomer shifts (δ), quadrupole shifts (E or E') and hyperfine field (H_{eff}) are manifested in several overlapping absorption patterns. There are well defined six-line patterns, but these are broadened with the outermost peaks being affected the most. The broadened lines are usually a good indication of a distribution of hyperfine interaction and therefore, a number of inequivalent Fe sites. There is an asymmetry in the amplitude between the left and right hand set of

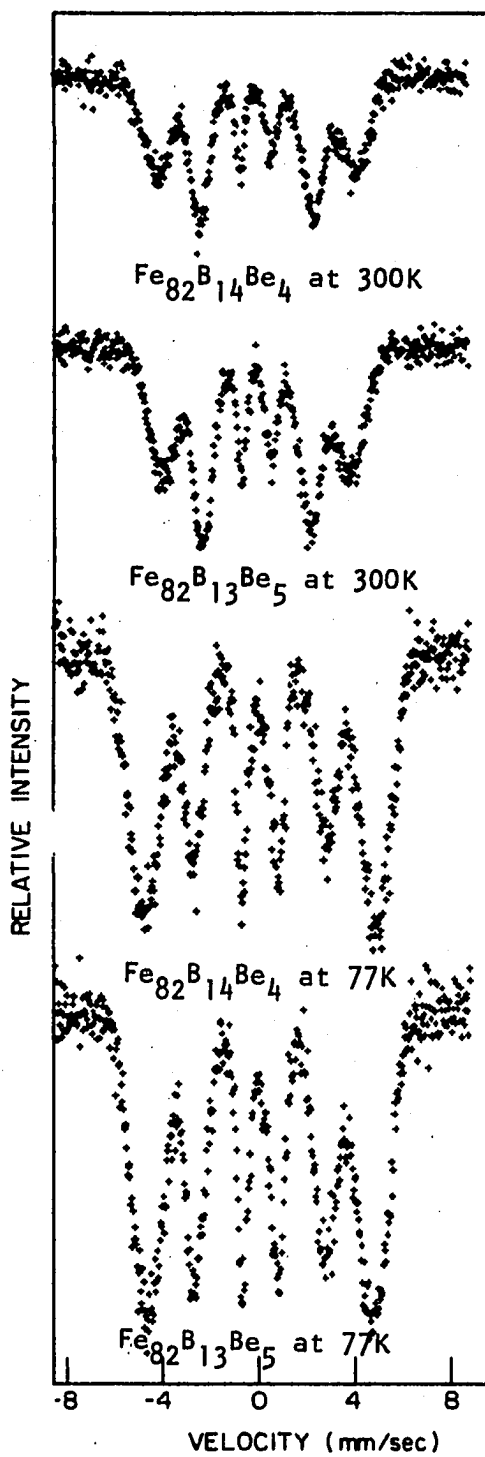


Figure 4. ^{57}Fe Mössbauer spectra of amorphous $\text{Fe}_{82}\text{B}_{14}\text{Be}_4$ and $\text{Fe}_{82}\text{B}_{13}\text{Be}_5$ at 300K and 77K

lines and this may be interpreted as a linear correlation between the isomer shift and the hyperfine splitting distributions (29).

The spectra were first analyzed using a six Lorentzian line fit to yield the average effective magnetic field, \bar{H}_{eff} , and the average isomer shift, $\bar{\delta}$, the values for which at 300K are displayed in Figures 5 and 6, respectively. There is an apparently discontinuity in the values of both \bar{H}_{eff} and $\bar{\delta}$ between $x=4$ and $x=5$. The corresponding values at 77K for \bar{H}_{eff} (Figure 7) and $\bar{\delta}$ (Figure 8) still indicate significant changes between $x=4$ and $x=5$, although the magnitude of the changes is less at 77K, an effect which may be attributed to a decrease in the spin-wave stiffness constant in the alloy with 5 at.% Be. (See section C-3.) However, the differences in the \bar{H}_{eff} values at 77K and 300K for all the samples containing Be are large compared to those of crystalline ferromagnets. For example, \bar{H}_{eff} for $\text{Fe}_{87}\text{B}_{14}\text{Be}_4$ is 295 kOe at 77K and 254 kOe at 300K while the corresponding change in \bar{H}_{eff} for iron is about 7 kOe. Chien (7) has attributed this difference to an increased excitation of long wavelength spin waves in amorphous ferromagnets compared to crystalline ferromagnets. On a Rhodes-Wohlfarth plot of p_C/p_S vs. T_C , where p_S is the saturation moment per magnetic atom and p_C is the effective moment per atom deduced from the Curie constant,

$$C = N_0 \mu_B^2 p_C (p_C + 2) / 3k_B, \quad (9)$$

this would imply that the crystalline ferromagnets would be closer to the local limit of 1 than would the $\text{Fe}_{82}\text{B}_{18-x}\text{Be}_x$ alloys (30).

The Mössbauer data were also analyzed in terms of a distribution of the magnetic hyperfine field by the Window method (31, 32, 33) which

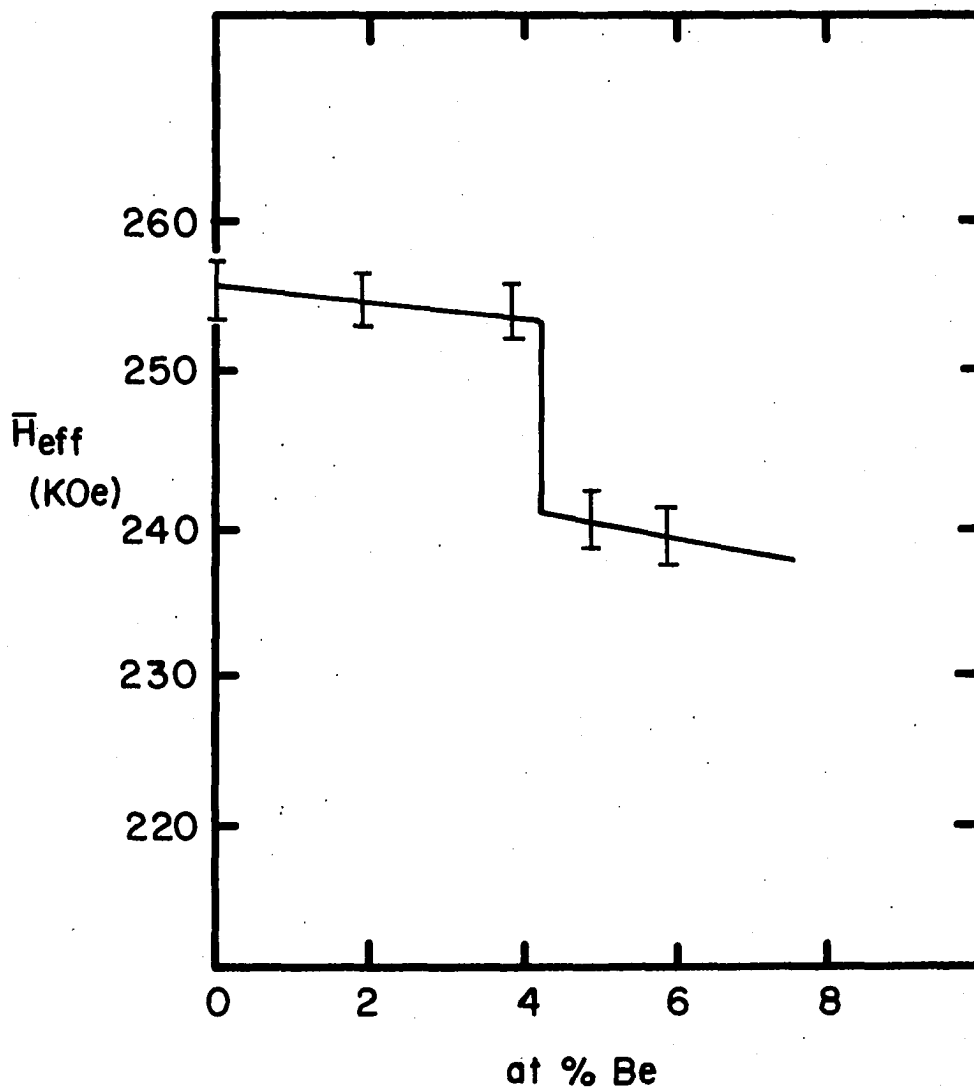


Figure 5. The average effective magnetic hyperfine field of amorphous $\text{Fe}_{82}\text{-B}_{18-x}\text{Be}_x$ alloys at 300K

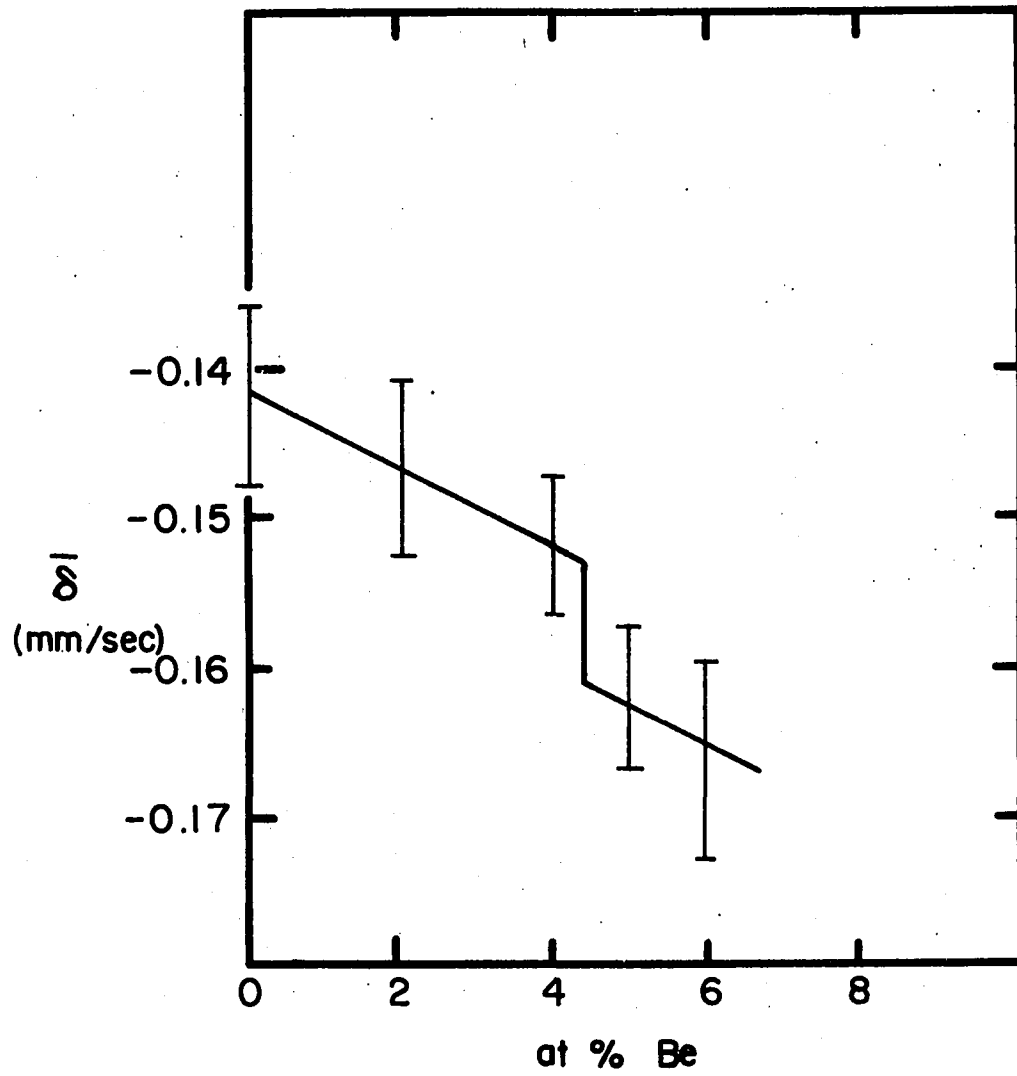


Figure 6. The isomer shift of amorphous $\text{Fe}_{82}\text{B}_{18-x}\text{Be}_x$ alloys at 300K

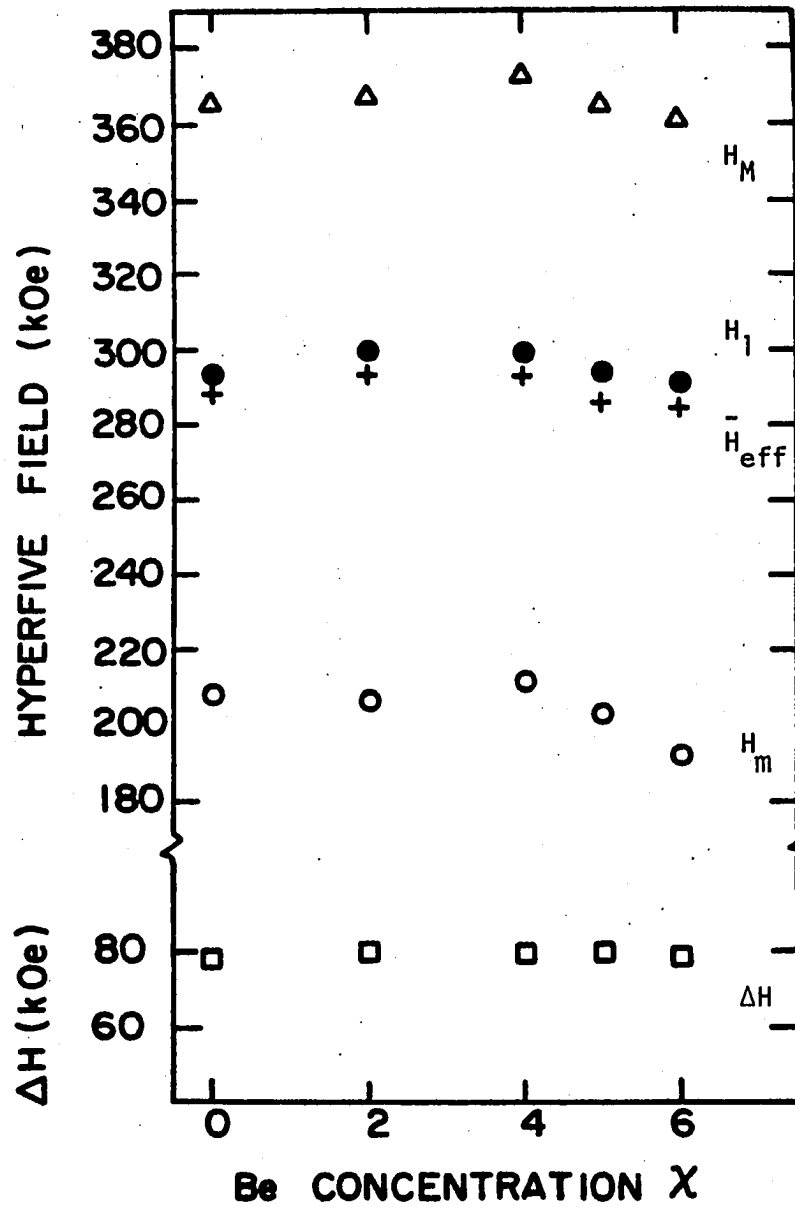


Figure 7. Concentration dependence of the various parameters of the ^{57}Fe hyperfine field distribution function $P(H)$ in amorphous $\text{Fe}_{82}\text{B}_{18-x}\text{Be}_x$ ($0 \leq x \leq 6$) at 77K: H_1 = effective magnetic hyperfine field, H_{eff} = average effective magnetic hyperfine field; H_m and H_M = effective hyperfine fields at which $P(H) \rightarrow 0$ on low and high fields sides of $P(H)$; ΔH = width of $P(H)$

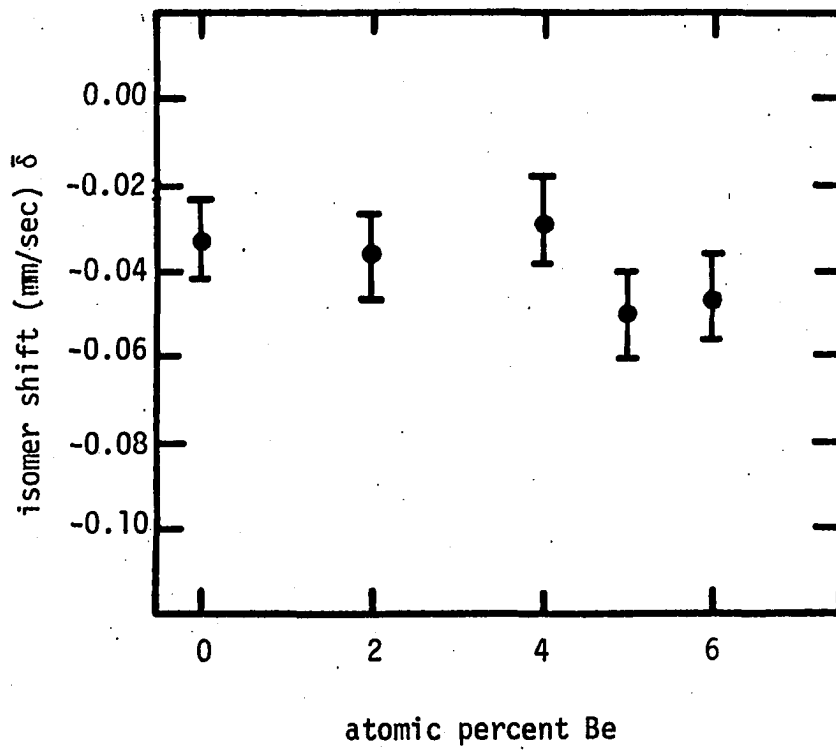


Figure 8. The isomer shift of amorphous Fe₈₂B_{18-x}Be_x alloys at 77K

assumes that quadrupole splittings and isomer shift effects on the broadening of the peaks in the spectra are negligible. Intermetallic compounds of transition metal-metalloid compounds show only minor variation in isomer shift (34), and Chien (7) has indicated that there is almost no apparent quadrupole interaction for an amorphous magnetic ordered solid. (However, it must be mentioned that Ok and Morrish (35) have also shown that broadening caused by the distribution of quadrupole splitting is not negligible in $\text{Fe}_{82}\text{B}_{12}\text{Si}_6$.) From resultant distribution functions of the effective magnetic field, $P(H)$, obtained by Fourier series expansion, the most probable value of the effective magnetic hyperfine field, H_1 , was obtained for each of the $\text{Fe}_{82}\text{B}_{18-x}\text{Be}_x$ alloys. These values are shown in Figure 7 together with the width of $P(H)$, ΔH , and values of H_m and H_M which are the effective magnetic hyperfine fields at which $P(H)$ approaches zero on the low-field and high-field side of the distribution function, respectively. From Figure 7, it can be seen that all these values, except for ΔH which remain constant at 80 kOe, follow the trend observed in the average magnetic moment ($\bar{\mu}_{\text{Fe}}$), \bar{H}_{eff} and $\bar{\delta}$ as the Be content is changed. Further details on the significance of the parameters obtained by the Window procedure are given elsewhere (36). The proportional behavior of the $\bar{\mu}_{\text{Fe}}$ and \bar{H}_{eff} has also been noted in both crystalline and amorphous Fe-metalloid systems (37, 38, 39). If it is assumed that the charge transfer observed in the alloys with $x \ll 4$ is from Be to Fe, then the increase in $\bar{\mu}_{\text{Fe}}$ and \bar{H}_{eff} may be explained in terms of the Stoner band model (40). Even though the density of states is large near the Fermi level and it is energetically favorable to have a large number of unpaired electrons, i.e., a large exchange energy

splitting, the maximum possible magnetism may not be obtained because the number of electrons is less than the optimal amount. Furthermore, the shape of the density of states and the concentration of electrons are dependent on composition (40). The transferred electrons may go to the spin up or spin down substates and the relative amount of charge transfer determines whether $\bar{\mu}_{\text{Fe}}$ and \bar{H}_{eff} will increase. In the alloys with $x \leq 4$, it can be assumed that the charge transfer served to increase the exchange splitting.

The isomer shift in ^{57}Fe is related to a change in the 3s electron density resulting from the change in the shielding effect of the 3d electrons (41). The isomer shift becomes more negative as the 3s electron density is increased and this increase can result from a decrease in 3d electron density. Therefore, the change in the isomer shift values of -0.032 mm/sec for samples with $x \leq 4$ to -0.050 mm/sec for samples with $x > 4$ is understandable if it is assumed that because there is no charge transfer from Be to Fe for samples with $x > 4$ (42) the 3d electron density is lower in these alloys compared to that in alloys with $x \leq 4$. The isomer shift reflects the state of the chemical environment, and the change in the local coordination number and Fe-Fe interatomic distance detected in these alloys (Section C-3) is sufficient to affect $\bar{\delta}$. Also, Hasegawa (43) has attributed the changes in the density of Fe-B-Be alloys to a change in the sites that the Be atoms occupy as the Be content is changed.

b. Crystallization products The Mössbauer spectrum at 300K for $\text{Fe}_{82}\text{B}_{18}$ annealed at 693K for 3 hours is shown in Figure 9a. From data of the X-ray experiments, an α -Fe phase is one of the phases that is expected

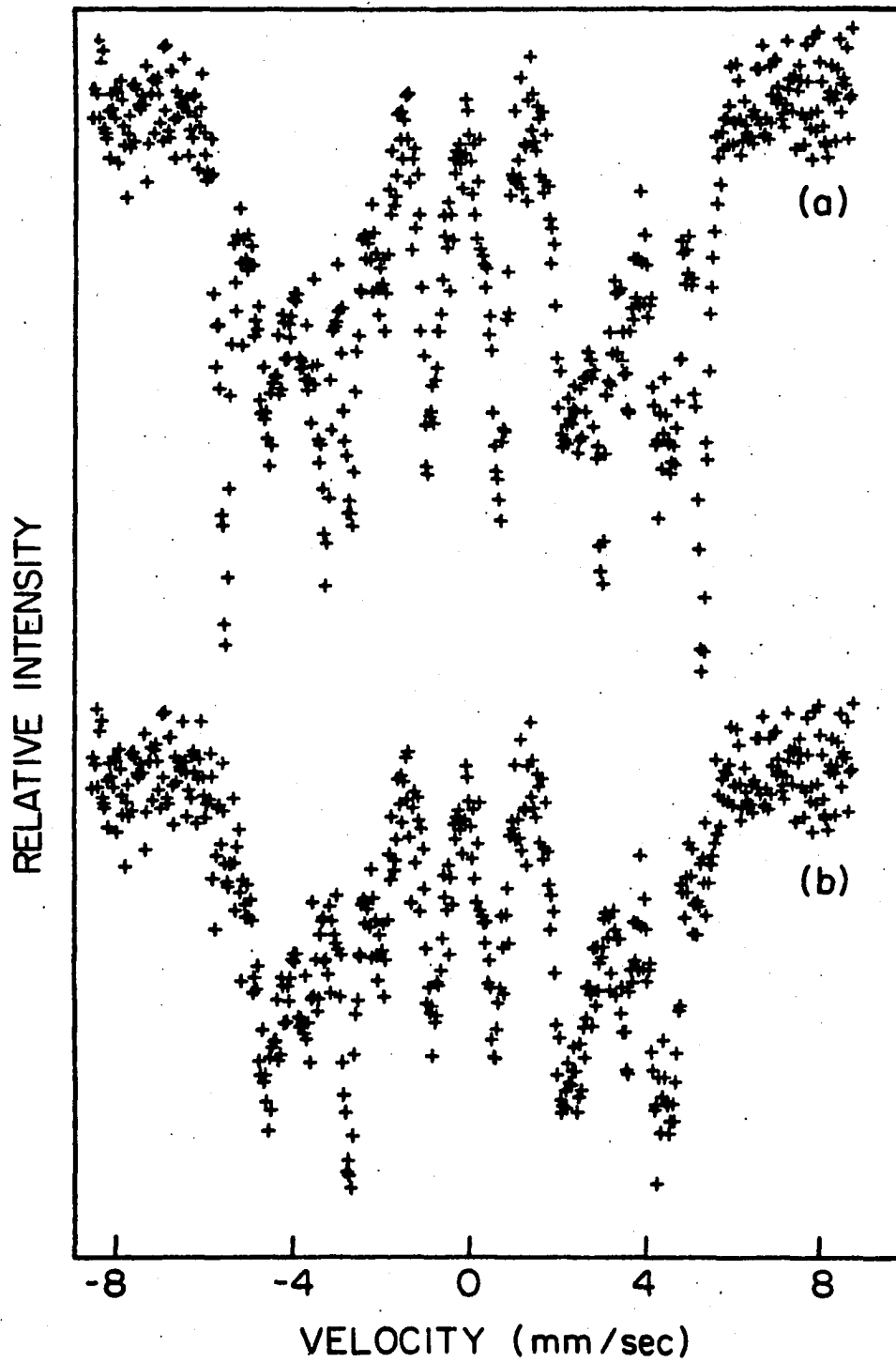


Figure 9. (a) ^{57}Fe Mössbauer spectrum of amorphous $\text{Fe}_{82}\text{B}_{18}$ at 300K after annealing at 693K for 3 hours. (b) the spectrum of the remaining phase after subtracting the α -Fe contribution

to emerge after the ribbons are annealed at 693K which is 20K higher than the crystallization temperature. Figure 9b is the Mössbauer spectrum which results when the α -Fe contribution is subtracted from the spectrum of Figure 9a. From the X-ray data and from a comparison of the spectrum in Figure 9b with that published for tetragonal Fe_3B (38), it can be concluded that the $\text{Fe}_{82}\text{B}_{18}$ undergoes a one stage crystallization resulting in the α -Fe and Fe_3B crystallization phases.

When Be is added to $\text{Fe}_{82}\text{B}_{18}$, two crystallization stages are observed. The spectra for $\text{Fe}_{82}\text{B}_{14}\text{Be}_4$ and $\text{Fe}_{82}\text{B}_{13}\text{Be}_5$ samples annealed for 3 hours at 693K, which is between T_{x1} and T_{x2} , are shown in Figure 10. Six sharp α -Fe lines together with six more broadened lines were present, the latter lines indicative of an amorphous phase. However, there are low intensity satellite lines in the region near the inner side of the α -Fe outermost lines. Such satellite lines are characteristic features of dilute solid solutions of Fe-base alloys with the solute occupying substitutional sites (44, 45, 46). Mössbauer spectra of solid solutions of Fe_9Be_3 and Fe_3Be_7 were obtained and compared with those shown in Figure 10. From the similarity in the spectra and also from the X-ray data in Table 3, it can be concluded that the α -Fe phase contains Be. The compositions of the α -Fe-Be solutions in the annealed $\text{Fe}_{82}\text{B}_{18-x}\text{Be}_x$ were determined from the intensity ratio of the satellite lines and corresponding outer Fe line and using the expression (47),

$$P(c,n) = \binom{8}{n} (1-c)^n c^{8-n} \quad (10)$$

which gives the probability that an iron in a bcc matrix has n nearest neighbors for a given Be concentration, c . The Fe_9Be_3 and Fe_3Be_7 were

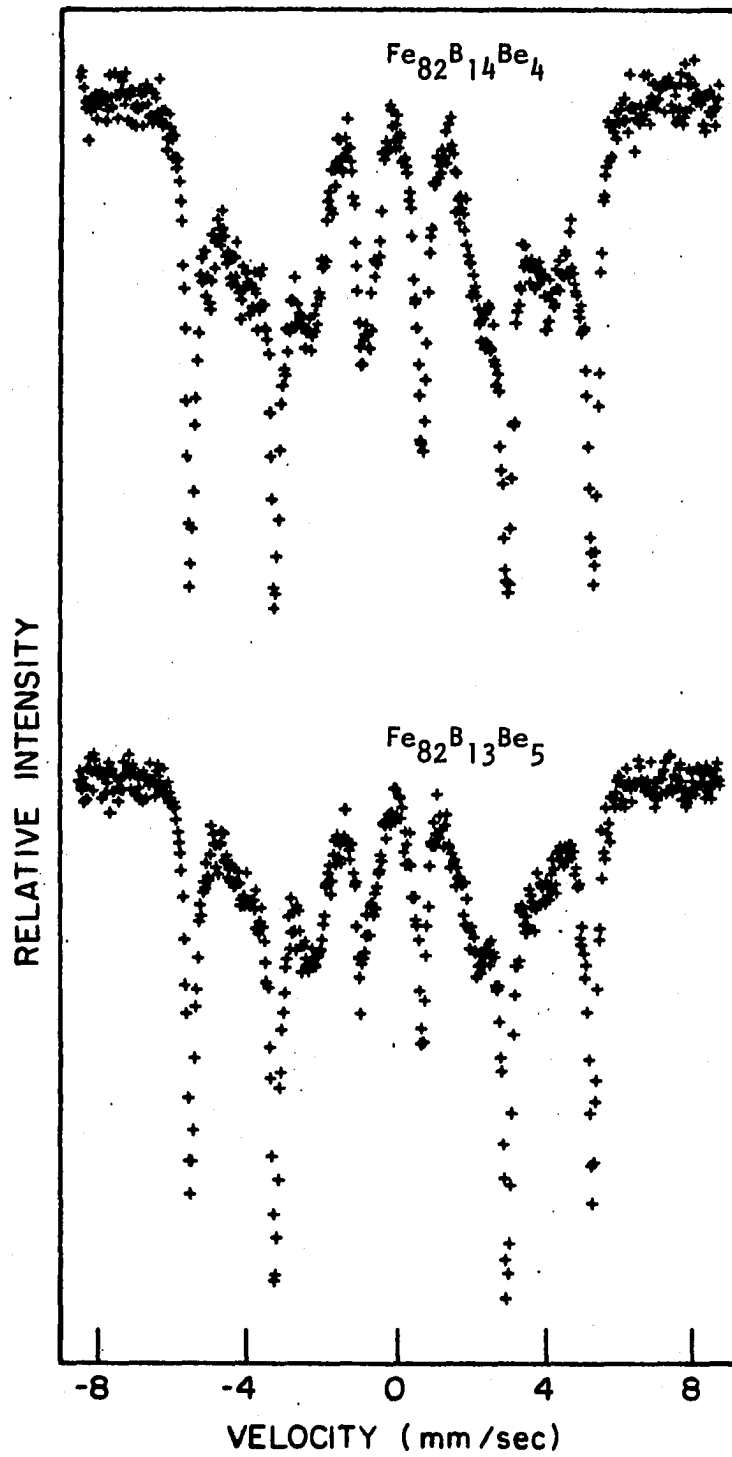


Figure 10. ^{57}Fe Mössbauer spectra of amorphous $\text{Fe}_{82}\text{B}_{14}\text{Be}_4$ and $\text{Fe}_{82}\text{B}_{13}\text{Be}_5$, at 300K after annealing at 693K for 3 hours

used as standards. The Be content in α -Fe-Be solid solutions was determined to vary from 3.5 to 5 at.%.

The samples annealed for 2 hours at 758K ($20K > T_{x2}$) yielded the Fe_2B intermetallic phase. Figure 11 shows the Mössbauer spectra for $Fe_{82}B_{14}Be_4$ and $Fe_{82}B_{13}Be_5$ samples annealed at 758K, in which the well-defined six-line pattern for the α -Fe-Be solid solutions together with a six-line pattern with smaller splitting that is due to Fe_2B , can be seen. The intensity ratio of the satellite lines to the outer α -Fe-Be lines is now reduced, indicating a lower Be content due to more Fe having precipitated out of the metastable amorphous phase. The reduction in the lattice constant of the Fe-Be obtained from the X-ray data (Table 3) confirmed this effect (24).

The relative intensity ratio of the Mössbauer absorption lines is related to the magnetic anisotropy. As is discussed in more detail elsewhere (36), the magnetization is aligned close to the ribbon plane for the samples annealed between T_{x1} and T_{x2} , but it is randomly oriented for samples annealed beyond T_{x2} . This effect can be attributed to a reduction in the lattice strain when the metastable amorphous phase present below T_{x2} is crystallized at temperatures beyond T_{x2} .

Note: The Mössbauer spectroscopy work on this section was done in collaboration with M. C. Lin of the Solid State Physics Division of Ames Laboratory, who performed the Mössbauer experiments. Further details may be found in a journal article entitled, "Mössbauer Effect Study of Iron-Boron-Beryllium Metallic Glasses," by M. C. Lin, C. S. Severin, R. G. Barnes, and C. W. Chen, to be published in Physical Review B.

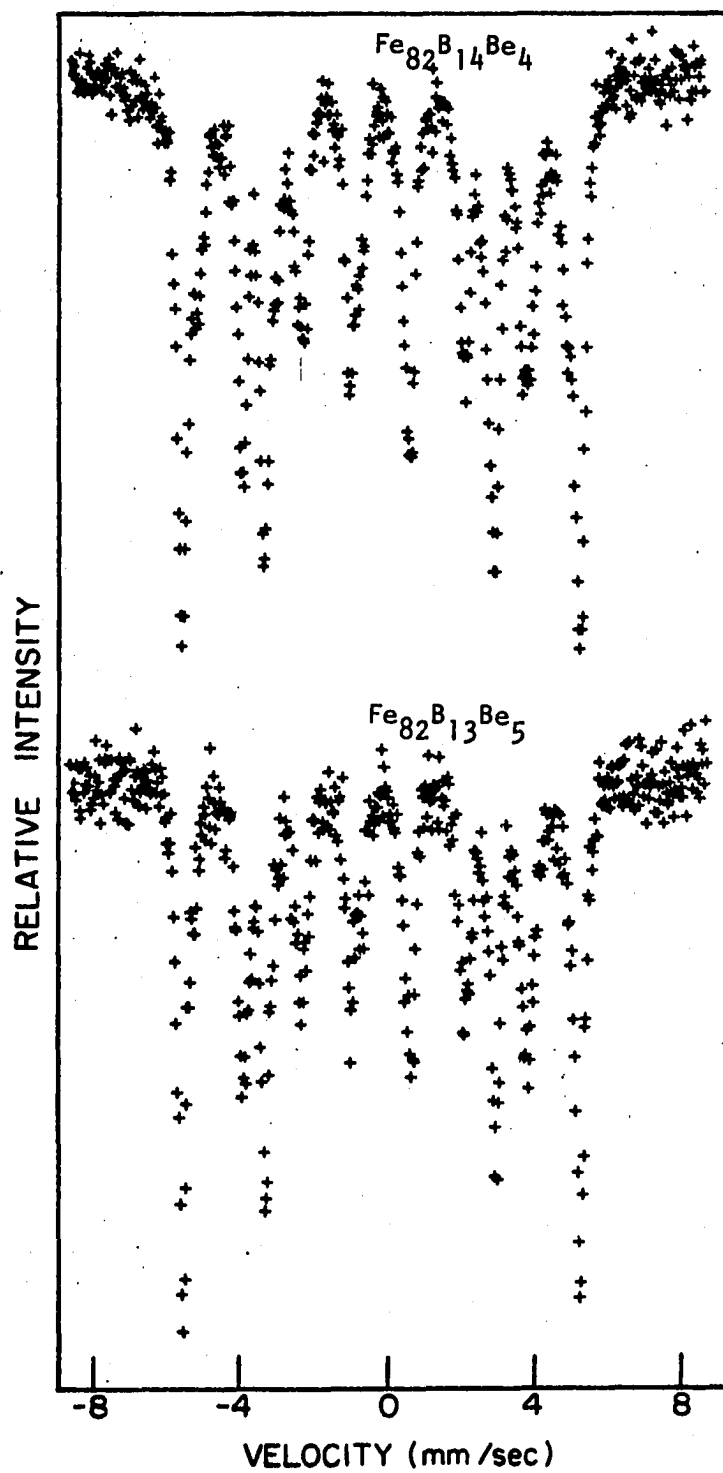


Figure 11. ^{57}Fe Mössbauer spectra of amorphous $\text{Fe}_{82}\text{B}_{14}\text{Be}_4$ and $\text{Fe}_{82}\text{B}_{13}\text{Be}_5$ at 300K after annealing at 758K for 2 hours

4. A discussion of charge transfer and the magnetic moment

In order to understand the effect of Be on the average Fe moment, we must first understand the role played by B. In both the Auger spectra shown in Figures 2 and 3, a peak occurs on the shoulder of the B escape peak at about 10 eV below the B KVV transition (180 eV). Such a peak is absent in the spectrum for elemental B. To explain this result, we recall that in the X-ray photoemission work of Matsuura et al. (48) on amorphous Fe-B, a small hump was seen in the intensity versus binding energy plot at about 10 eV below the Fermi level. The latter authors attributed this hump to a newly created bonding state between the 2p electrons of B and the 3d electrons of Fe. The existence of such a bonding state had previously been postulated for transition metal-transition metal alloys by Terakura and Kanamori (49) and for transition metal-hydrogen alloys (50). We, therefore, attribute the small peak in our Auger results to a hybridization of the B 2p and the Fe 3d electrons. We further attribute the decrease in the average Fe moment observed in both crystalline FeB (2) and amorphous Fe-B to such bonding. This explanation is, however, contrary to the theory that the decrease in the average Fe moment is caused by the filling-in of the Fe bands by the electrons transferred from the B (2). In this connection, it is worth noting that the existence of physical charge transfer in the TM-base metallic glasses is in dispute. O'Handley and Boudreaux (3), as well as Takacs (51), generally support the theory of actual charge transfer from the metalloid to Fe, Ni, or Co. They cite both theoretical and experimental studies which suggest the close packing of the metalloids in the interstices of the random TM structure and conclude that this requires the radii of the metalloids to

be smaller than their covalent radii, and therefore, charge transfer is suggested by such an arrangement. The problem of inferring bonding from interatomic distances alone is addressed by Corbett and Anderegg (52) based on the Pauling bond orders. Moreover, Pauling (53) himself supports the idea of charge transfer from the TM atom to the metalloids. Even the results of Brown and Cox (54), based on electron density maps derived from X-ray and neutron diffraction data indicate the transfer of valence electrons from B to the 4s states of Fe, not the 3d, in Fe_2B . Additionally, Alben et al. (55) dispute the theory of charge transfer from the metalloid to a transition metal on the basis of Switendick's (56) band theory calculation on Fe_3Si which shows the s and p orbitals of Si lying below the Fe Fermi level.

In view of the various arguments against the charge-transfer model, it is conceivable that in amorphous Fe-B there is a transfer of charge from the Fe d-orbitals. The emergence of a peak at ~ 170 eV in the Auger spectra and the small hump observed in the XPS spectra (48) may be taken as evidence for this type of charge transfer. A transfer of d-electrons from Fe can reduce the Fe average moment if the transfer has effectively reduced the splitting between the spin-up and spin-down levels. One may recall from the Pauling-Slater curves (57) for Fe-Co alloys that a reduction in the average number of outer electrons is accompanied by a reduction in the Fe average moment (10). Although the magnetic interactions which result in a change in the Fe moment in Fe-Co may not be applicable to the Fe-metalloid systems, the fact that a reduction in average Fe moment accompanying a reduction in the average outer electrons of Fe has been shown to occur in both alloy systems may be more than coincidental.

The exact mechanism leading to the decrease of $\bar{\mu}_{\text{Fe}}$ in the amorphous alloys containing Be is not known at present. Since no appreciable differences were seen in the B lineshape or the position of the B escape peak in the high resolution Auger spectra for Fe-B (58) and $\text{Fe}_{82}\text{B}_{18-x}\text{Be}_x$ alloys, it is reasonable to eliminate B and propose Fe as the receptor of the electrons transferred from Be when $x \leq 4$ in the ternary alloys. Then, if the electrons from Be cause an increase in the d electrons of Fe, this may be reflected in the observed increase of the average Fe moment. When the Be content is greater than 4 at.%, charge transfer from Be suddenly ceased, and both the number of d electrons per Fe atom and the average Fe moment began to decrease.

We have not yet addressed the problem as to why Be transfers electrons for $x \leq 4$ and does not do so for $x > 4$. We know that a change in the local environment and the thermodynamic stability can influence the physical properties of an alloy. The Mössbauer data indicate there is a change in the local environment of the Fe atoms, but this evidence is indirect from the hyperfine field, whose value is averaged over many interatomic distances. However, Hasegawa (43) has reported changes in density and magnetostriction in $\text{Fe}_{80}\text{B}_{20-x}\text{Be}_x$ and $\text{Fe}_{82-y}\text{Be}_y\text{B}_{18}$ metallic glasses when the Be content exceeds ~ 4 at.%. Also, a concentration dependence has been observed for various physical properties in amorphous Fe-B, such as a change in density (59, 60), a change in the coordination number for the Fe atom (15) and a change in the average Fe moment (61, 62). Based on these results and the RDF results in Part C, we may attribute the change in the behavior of Be to a change in the position it occupies in the amorphous structure. For $x \leq 4$, the Fe matrix could be

thought to be saturated with B atoms in the first shell. This is inferred from the work on Fe-B where the idea of saturation of the first shell is deduced from the density data (59, 60) when the B to Fe atomic ratio is greater than 0.16, as it is in $\text{Fe}_{84}\text{B}_{16}$ and $\text{Fe}_{82}\text{B}_{14}\text{Be}_4$.

In Fe-metallic glasses, a direct relation between the nearest coordination number (n_1) and the average Fe magnetic moment ($\bar{\mu}_{\text{Fe}}$) has been established (15). It was shown that around 14 to 16 at.% B, both n_1 and $\bar{\mu}_{\text{Fe}}$ go through a maximum. When the B concentration falls below the above values, both n_1 and $\bar{\mu}_{\text{Fe}}$ decrease. As is discussed in Part C of this section, the n_1 value drops drastically from 10.5 for $\text{Fe}_{82}\text{B}_{14}\text{Be}_4$ to 9.1 for $\text{Fe}_{82}\text{B}_{13}\text{Be}_5$. This change in n_1 supports the theory that a structural change occurs to cause a corresponding change in Fe magnetic moment. For the Be content of ≤ 4 at.% ($\text{B} \geq 14$ at.%), the Be atoms may be lying outside the first Fe-Fe shell. This idea is supported by the RDF data (reported in Part C) which shows no change in the Fe-Fe interatomic spacing for $\text{Fe}_{82}\text{B}_{14}\text{Be}_4$ when compared to $\text{Fe}_{87}\text{B}_{13}$. With a decrease in the B content (and an increase in Be content beyond 4 at.%), the B occupancy is decreased and the Be atoms may now occupy a shell closer to the Fe atoms. The reduction of the lattice strain as a result of Be atoms replacing B atoms and the decrease in n_1 may be responsible for the decrease in the Fe-Fe interatomic spacing seen in the RDF work on $\text{Fe}_{82}\text{B}_{13}\text{Be}_5$. The Auger results on $\text{Fe}_{97}\text{Be}_3$ and $\text{Fe}_{93}\text{Be}_7$ crystalline alloys have shown that the Be KVV transition occurs near 106 eV, similar to what is observed in $\text{Fe}_{82}\text{B}_{13}\text{Be}_5$ when no charge transfer is observed. Therefore, we may conclude that the change in the Be behavior from an initial transfer of charge to no charge transfer as the Be content is increased is a direct

result of a change in the local environment of Fe atoms.

B. Fe-B-Au

1. Magnetic and thermomagnetic behavior

The saturation magnetization M_s at 4.2K and 18 kOe of $\text{Fe}_{82}\text{B}_{18-x}\text{Au}_x$ metallic glasses are 196, 200, 198, and 201 emu/g for the nominal values of $x=0, 0.5, 1.0,$ and $1.5,$ respectively. These M_s values can be converted to average Fe moments μ_{Fe} by assuming that Fe is the only magnetic species and by using the analyzed composition of the alloys. The $\bar{\mu}_{\text{Fe}}$ increased from $2.05 \mu_B$ for $x=0$ ($\text{Fe}_{82}\text{B}_{18}$) to $2.20 \mu_B$ for $x=1.5$, indicating a significant beneficial effect of Au on $\bar{\mu}_{\text{Fe}}$. The M vs. T behavior of $\text{Fe}_{82}\text{B}_{18}$ is displayed in Figure 12. The Curie temperature of 644K and the crystallization temperature of 673K are in good agreement with published data for this alloy (21). Our identification by Mössbauer spectroscopy of the crystalline products as α -Fe and Fe_3B is also in agreement with previous work (38, 62). When Au partially replaces B, as in $\text{Fe}_{82}\text{B}_{17.5}\text{Au}_{0.5}$, an additional crystallization stage is seen (Figure 13). The crystallization products in this alloy are now α -Fe with a small percentage of Au (referred to as α -Fe(Au)) for stage I and Fe_2B for stage II. The X-ray results showed no evidence of Fe_3B at any of the two stages.

The M vs. T behavior for $\text{Fe}_{87}\text{B}_{11}\text{Au}_2$ is shown in Figure 14. The profile is similar to that shown for $\text{Fe}_{82}\text{B}_{17.5}\text{Au}_{0.5}$, except that three distinct crystallization stages are now seen. From the X-ray data listed in Figure 15 (Co radiation, Debye-Scherrer method), the crystalline phases are identified as a solid solution of α -Fe with Au, Fe_2B , and a Au-rich solid solution with Fe. The crystallization sequence is described below.

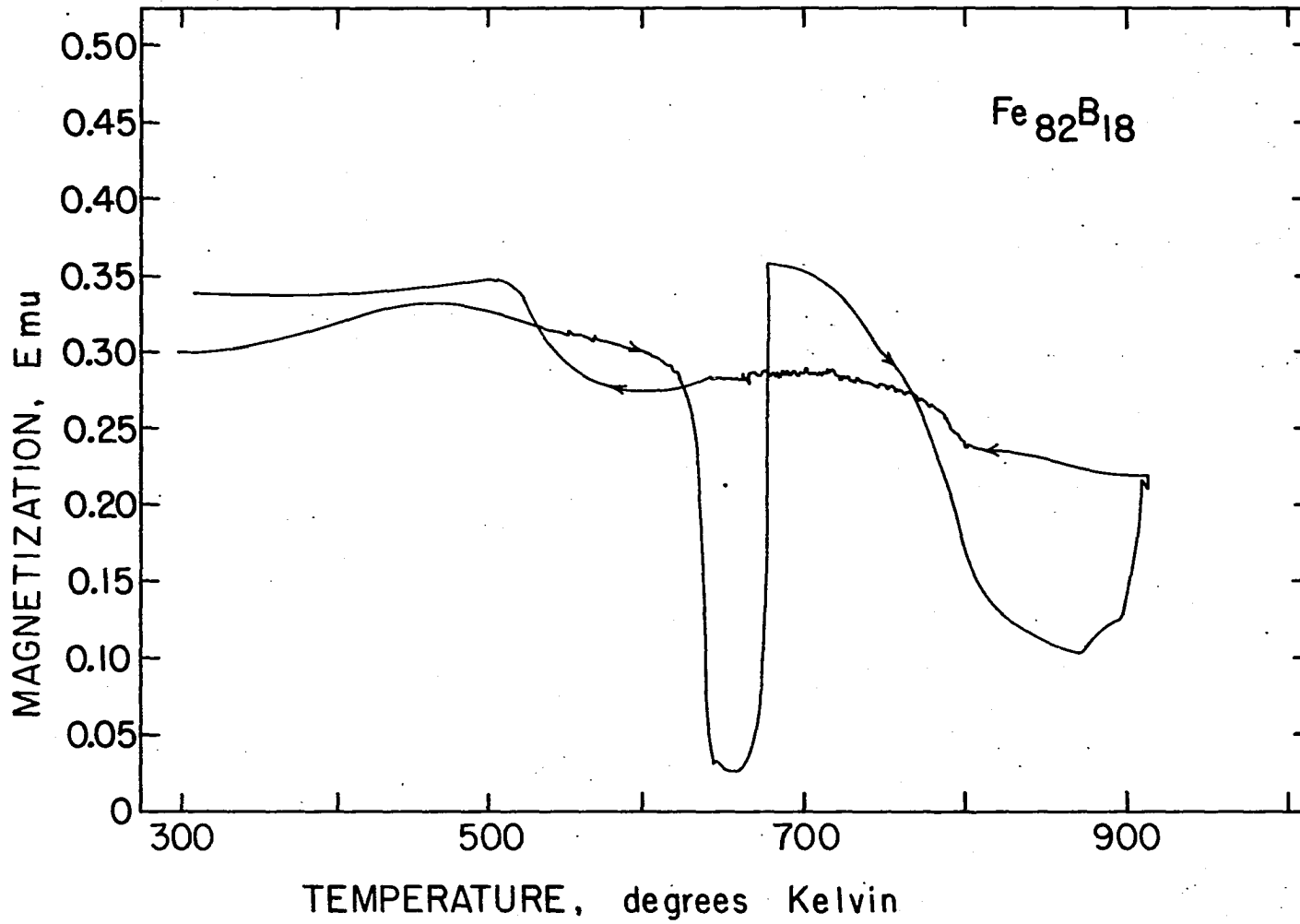


Figure 12. Annealing behavior of Fe₈₂B₁₈ (applied field = 50 Oe)

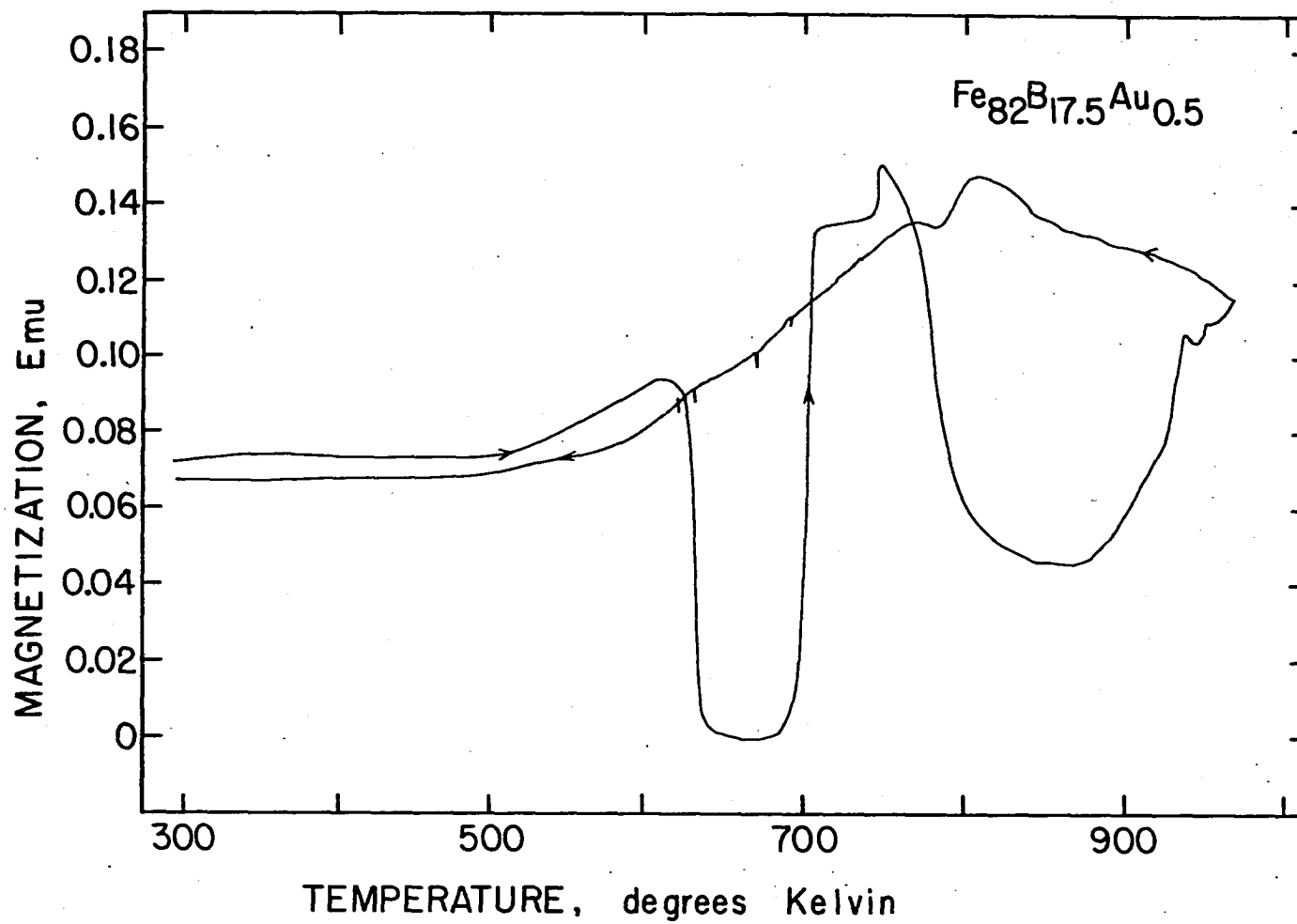


Figure 13. Annealing behavior of $\text{Fe}_{82}\text{B}_{17.5}\text{Au}_{0.5}$ (applied field = 50 Oe)

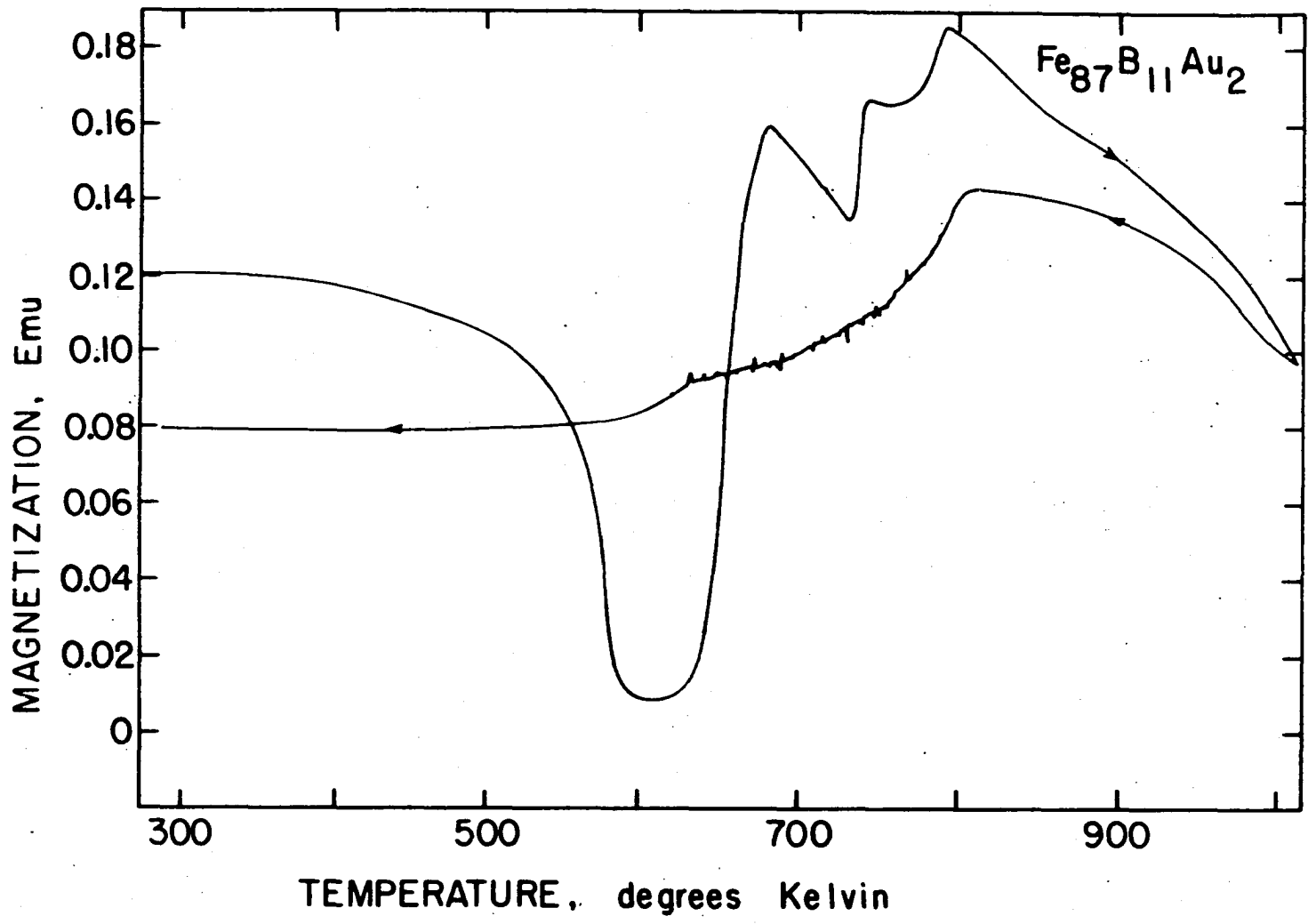


Figure 14. Annealing behavior of $\text{Fe}_{87}\text{B}_{11}\text{Au}_2$ (applied field = 50 Oe)

Annealing Temperature																			
618K	d			2.0313	2.0302				1.4359	1.1722	1.0158								
	I			5	100				25	50	20								
	hkl			1108	110				200	211	220								
	phase			A	A				A	A	A								
649K	d			2.0214	2.0285				1.4351	1.1716	1.0146								
	I			5	100				25	45	20								
	hkl			1108	1108				1108	1108	1108								
	phase			A	A				A	A	A								
678K	d			2.0286	2.0319				1.4355	1.1720	1.0148								
	I			5	100				25	50	20								
	hkl			1108	110				200	211	220								
	phase			A	A				A	A	A								
708K	d			2.0153	2.0353				1.4368	1.1723	1.0747								
	I			5	100				25	50	20								
	hkl			1108	110				200	211	220								
	phase			A	A				A	A	A								
753K	d	3.6339		2.1028	2.0310	2.0325		1.8170	1.6283		1.1735	1.0503	1.0162						
	I	5		10	10	100		2	15		70	1	40						
	hkl	110		002	1108	110		112	202		211	332	220						
	phase	B		B	A	A		B	B		A	B	A						
793K	d	3.6399		2.3302	2.1082	2.0330	2.0349	1.8219	1.6285	1.4367	1.1728	1.0153	1.0022						
	I	6		6	10	15	100	2	20	40	60	40	2						
	hkl	110		111	002	1108	110	112	202	200	211	220	400						
	phase	B		C	B	A	A	B	B	A	A	A	C						
884K	d	3.6335	2.5565	2.3232	2.1130	2.0285	2.0328	2.0115	1.8200	1.6831	1.4353	1.4182	1.1716	1.0483	1.0144	1.0140	1.0025	0.9074	0.9073
	I	5	5	40	10	10	100	5	3	20	40	2	60	3	30	15	3	50	20
	hkl	110	200	111	002	1108	110	200	112	202	200	220	211	332	220 α_1	220 α_1	400	310 α_1	310 α_1
	phase	B	B	C	B	A	A	C	B	B	A	C	A	B	A	A	C	A	A

Figure 15. Annealing temperatures, d-spacings, intensities, I, crystallographic indices, hkl, and crystalline phases of the annealing products of Fe₈₇B₁₁Au₂. [A=α-Fe(Au); B=Fe₂B; C=Au(Fe)]

The X-ray diffraction patterns (Mo radiation) for the amorphous ribbons and for ribbons annealed for 25 minutes at 708K and 793K are shown in Figures 16, 17, and 18, respectively.

The magnetization vs. applied field (M vs. H) plot for the amorphous ribbon and ribbons annealed at various temperatures, T_a , is shown in Figure 19. The M_S values at 18 kOe are plotted versus T_a in Figure 20. Small decreases are seen in M_S for T_a below 723K. However, M_S drops rapidly above that temperature because of the formation of Fe_2B .

The comparatively large increase in μ_{Fe} , $\Delta\bar{\mu}_{Fe} = .15 \mu_B$, observed in $Fe_{82}B_{16.5}Au_{1.5}$ is much greater than expected from a decreased charge transfer effect. If this increase in $\bar{\mu}_{Fe}$ were due solely to charge transfer, the Au substitution would cause a depopulation of the Fe d-bands at a very high rate per Au atom. Moreover, the relatively high $\bar{\mu}_{Fe}$ displayed in $Fe_{87}B_{11}Au_2$ would cause the reduced charge transfer to be an unrealistic 16 electrons per Au atom. Clearly, the observed $\Delta\mu_{Fe}$ has its origins elsewhere. In this connection, we recall that Fe is known to exist in the bcc phase with $\bar{\mu}_{Fe} = 2.2 \mu_B$ and it also has an fcc phase with two electronic states, γ_1 and γ_2 , where γ_1 is a low-volume anti-ferromagnetic lattice ($a_0 = 3.54 \text{ \AA}$, $\bar{\mu}_{Fe} = 0.7 \mu_B$) and γ_2 is a high-volume ferromagnetic lattice ($a_0 = 3.64 \text{ \AA}$, $\bar{\mu}_{Fe} = 2.8-2.9 \mu_B$) (11, 12). Felsch (9) has reported an $\bar{\mu}_{Fe} = 2.9 \mu_B$ in amorphous films of Fe-Au with more than 6 at.% Au and the high moment has been attributed to the stabilization of a high-moment phase by the effect of the large Au atoms and the quenching-in-place effect of the rapidly cooled deposition of the Fe-Au films (13). It appears plausible to ascribe the increase in the average Fe moment observed in our amorphous alloys to the formation of a number of Fe-Fe

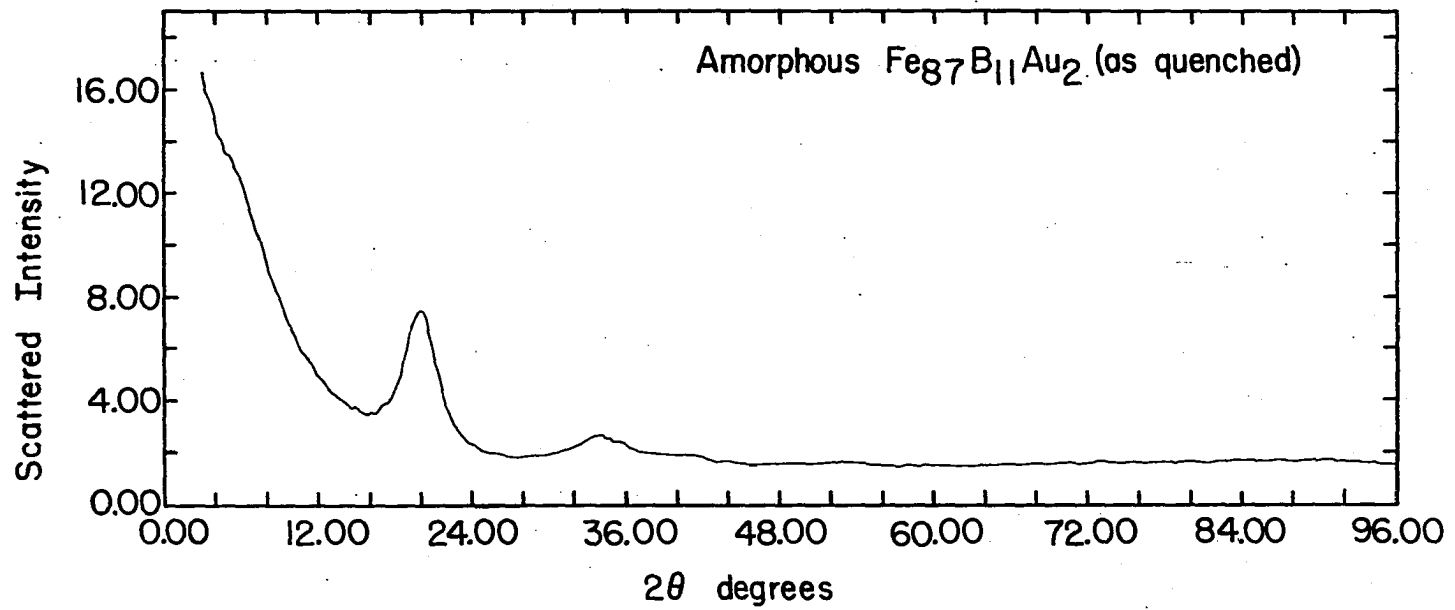


Figure 16. X-ray diffraction pattern for amorphous, as-quenched $\text{Fe}_{87}\text{B}_{11}\text{Au}_2$ ribbons

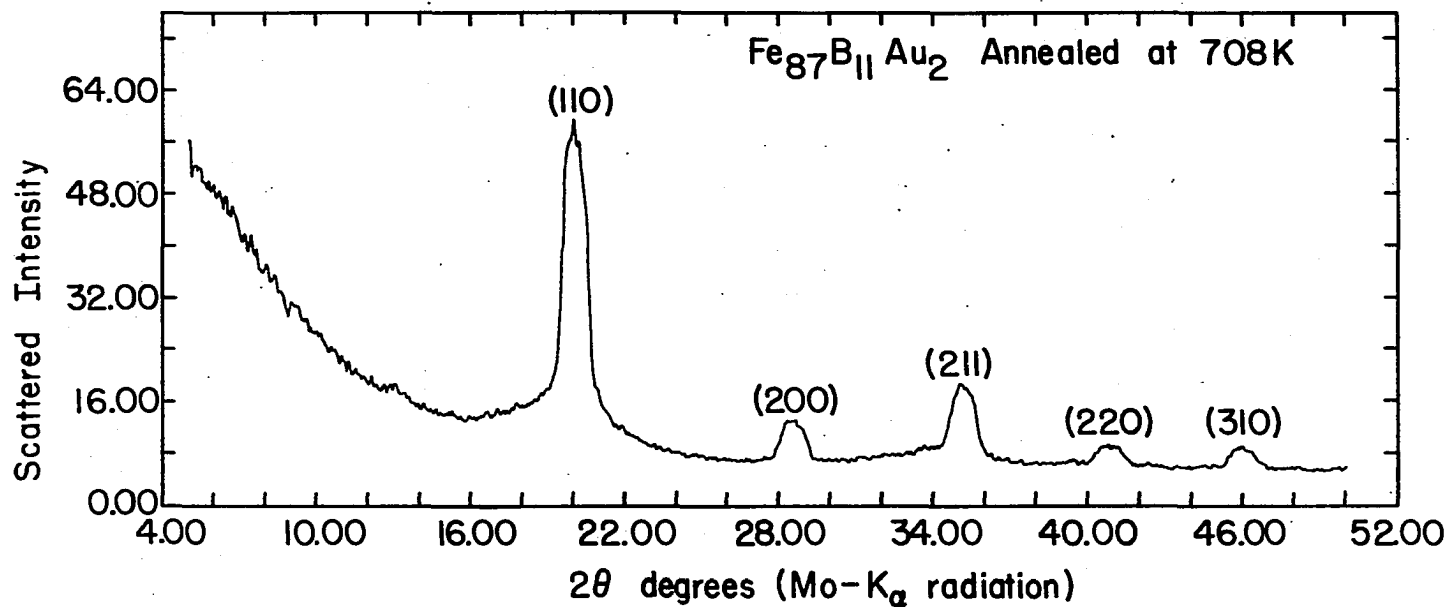


Figure 17. X-ray diffraction pattern for $\text{Fe}_{87}\text{B}_{11}\text{Au}_2$ ribbons annealed at 708K for 25 minutes

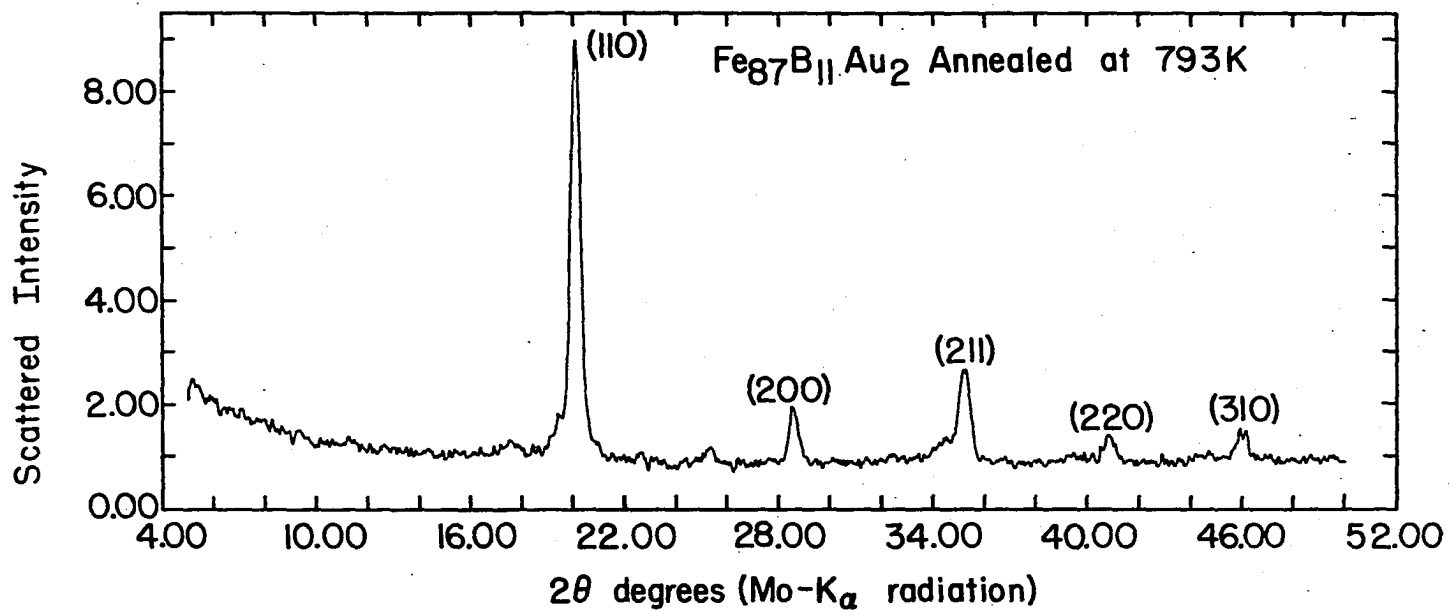


Figure 18. X-ray diffraction pattern for Fe₈₇B₁₁Au₂ ribbons annealed at 793K for 25 minutes

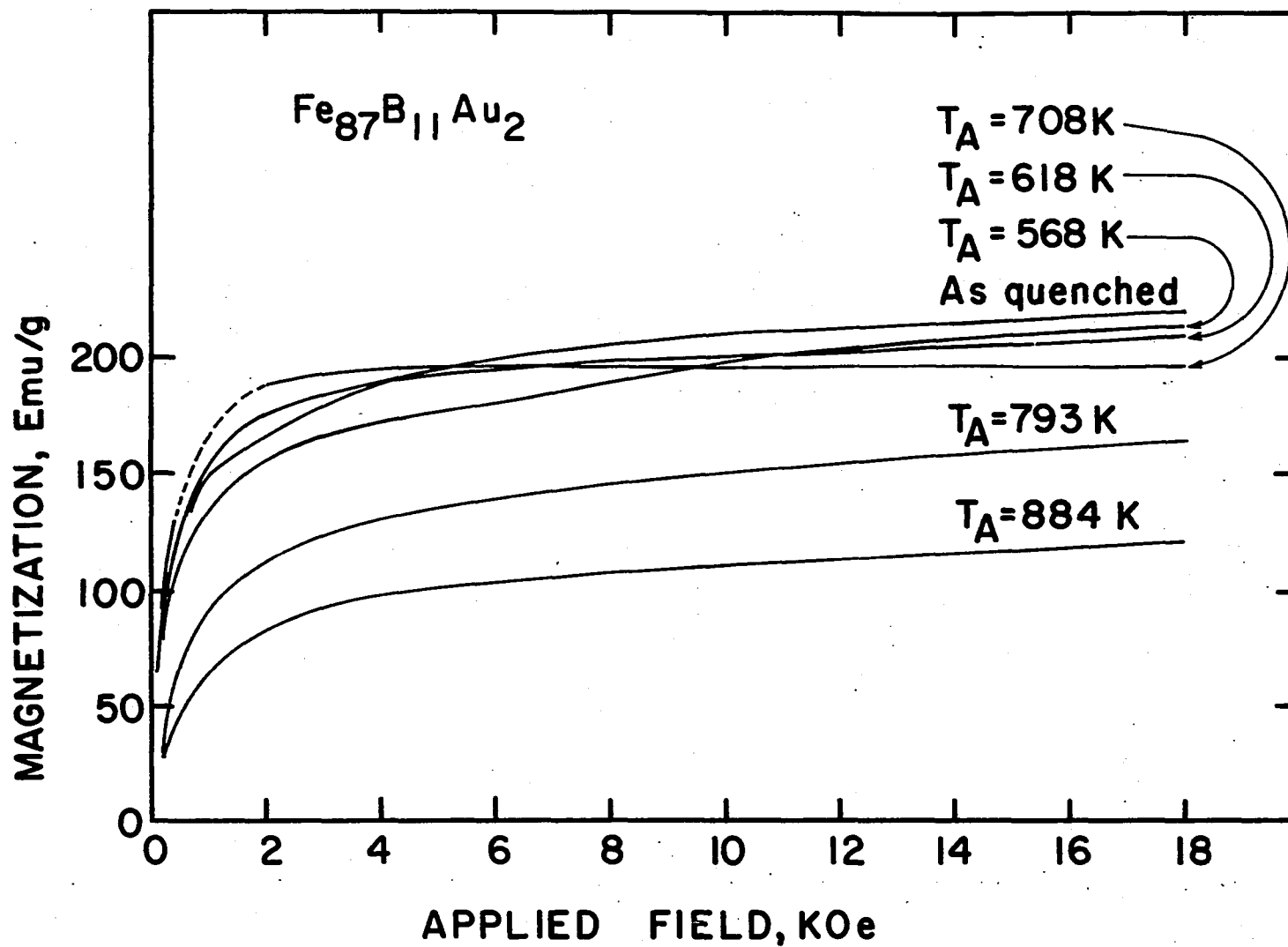


Figure 19. Magnetization vs. applied field for $Fe_{87}B_{11}Au_2$ ribbons annealed at temperatures indicated for 25 minutes

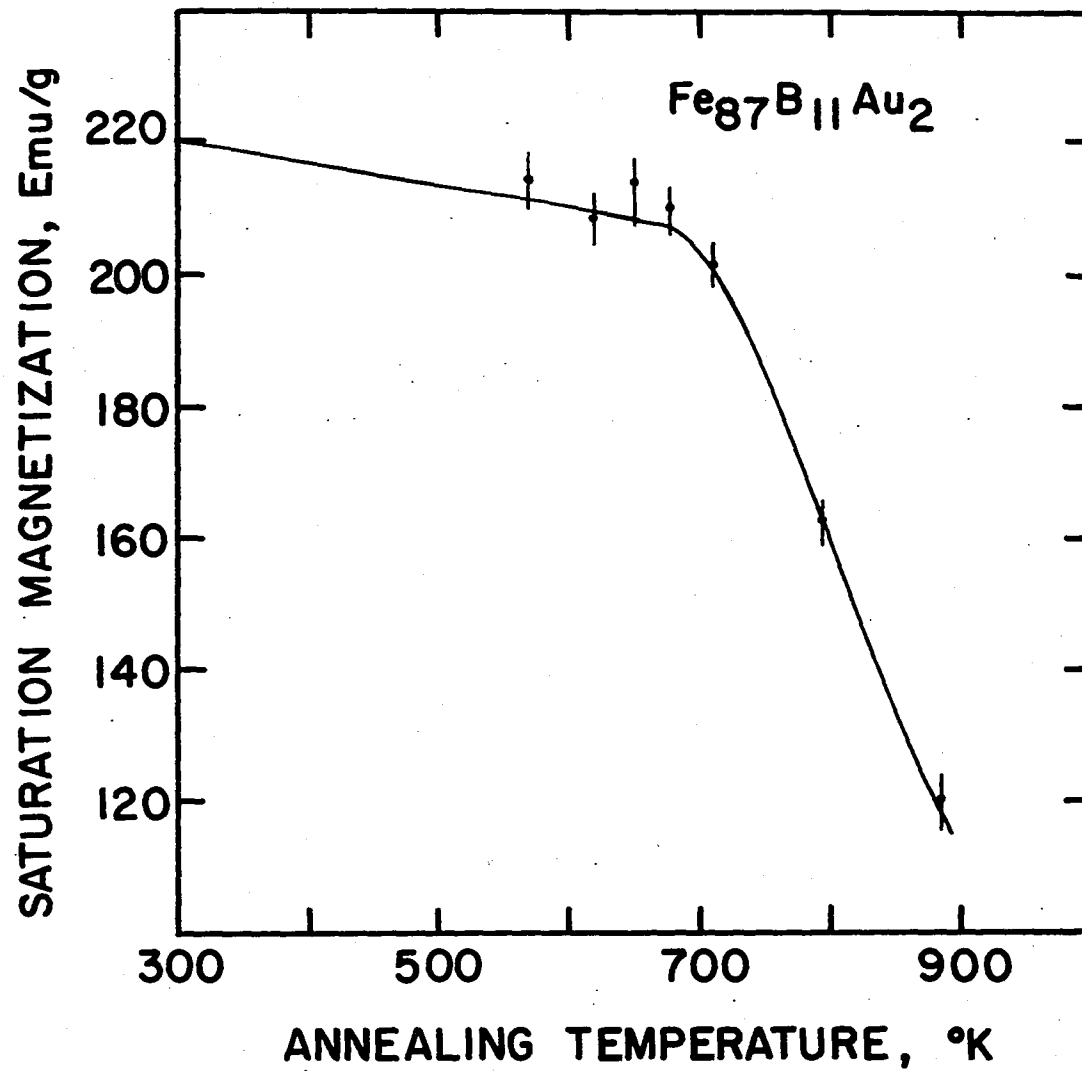


Figure 20. Saturation magnetization values at 18 kOe vs. annealing temperature for Fe₈₇B₁₁Au₂ ribbons

nearest neighbors with an interatomic spacing close to that of the large volume fcc γ_2 Fe lattice. The fact that more than 6 at.% Au was needed to obtain a $\bar{\mu}_{\text{Fe}}$ of $2.9 \mu_{\text{B}}$ in Fe-Au probably indicates that there is a distribution in the interatomic spacings when the Au content is less than 6 at.% and a distribution in Fe moments, leading to an average Fe moment of less than $2.9 \mu_{\text{B}}$. A distribution in the interatomic spacing, r , is an inherent characteristic of an amorphous structure, as is evidenced by the large full width at half-maximum of the peaks in the radial distribution functions. It is expected that increasing amounts of Au in Fe-B-Au will cause the position of the peaks for Fe-Fe nearest neighbors to shift to higher r , or at least cause a significant shoulder on the high r side of those peaks.

We may conclude that the $\bar{\mu}_{\text{Fe}}$ of $2.20 \mu_{\text{B}}$ observed in $\text{Fe}_{82}\text{B}_{16.5}\text{Au}_{1.5}$ and $2.46 \mu_{\text{B}}$ in $\text{Fe}_{87}\text{B}_{11}\text{Au}_2$ reflects a distribution of Fe moments as some of the Fe-Fe spacings are increased because of the presence of large Au atoms. It is expected that some of the Fe-Fe spacings will remain the same as those in Fe-B since B is the principal alloying element in the ternary alloys. The progressive decreases in the M_s (see Figures 19 and 20) as the annealing temperature is increased are consistent with the idea that the progressive formation of $\alpha\text{-Fe(Au)}$ means the formation of a phase with smaller Fe-Fe spacing and a lower M_s .

2. Crystallization of $\text{Fe}_{87}\text{B}_{11}\text{Au}_2$

The X-ray data shown in Figure 15 seem to indicate the following crystallization sequence in the $\text{Fe}_{87}\text{B}_{11}\text{Au}_2$ alloy.

Stage I. The amorphous alloy crystallizes into a major phase of

α -Fe(Au) solid solution with about 3 at.% Au and a minor metastable phase of an Au-rich solid solution containing about 40 at.% Fe; an amorphous Fe-B-Au phase is still a major part of the alloy:



The maximum rate of crystallization occurs around 660K. Marchal et al. (64) have observed, in crystallizing Fe-rich Fe-Au films, that initially a bcc metastable phase forms with weak segregation of an fcc Au-rich phase. We observed only one set of fcc (111) reflections, similar to their observations. The broadening of this reflection and those of the bcc phase in our alloy supports the idea of micro-segregation or fluctuations in concentration in the crystallizing process in $\text{Fe}_{87}\text{B}_{11}\text{Au}_2$, also consistent with their observations in Fe-Au.

The amount of Au in the α -Fe(Au) increases as the annealing temperature is increased up to 660K, apparently at the expense of the Au-rich phase. We could not detect by X-ray the presence of the Au-rich phase in the ribbons annealed above 649K. The ribbons annealed at 678K and 708K had less Au in the α -Fe(Au) phase. This decrease in Au content continued until the second crystallization stage is reached.

Stage II. Another crystalline phase Fe_2B emerges and grows out of the remaining amorphous Fe-B-Au with the maximum rate of growth occurring at 745K. This crystallization temperature is close to those observed for Fe_2B precipitation in the Fe-B-Be amorphous alloys. The increase in the lattice constant of the α -Fe(Au) indicates that the Au content increases at this stage, probably because Au is further released from the amorphous Fe-B-Au when the Fe_2B is being formed. This Au would dissolve into the

α -Fe matrix. Further annealing at higher temperatures then causes Au to be precipitated out of the α -Fe to form an Au-rich solid solution with Fe in Stage III.

Stage III. Ribbons annealed at 793K and 884K showed a third crystalline phase of an Au-rich solid solution. This is in agreement with the work on Fe-Au films (64) which indicated an Au-rich phase showing the large Au fcc lattice constant. The lattice spacing in our experiments was 1.3% less than that of pure Au, indicating perhaps the presence of Fe in this phase (65). However, Mössbauer spectroscopy could not detect any evidence for Fe in this phase. The lattice constant of α -Fe(Au) phase progressively decreased, approaching that of pure bcc Fe above 884K.

C. Atomic Arrangement Based on Radial Distribution Functions

1. Fe₈₇B₁₃

From the structure factor, the reduced radial distribution function, $G(r)$, defined as $4\pi r[\rho(r)-\rho_0]$, was evaluated by a Fourier transformation of the structure factor, $S(k)$ according to Eq. (6). The $G(r)$ curve for the binary alloy Fe₈₇B₁₃ is shown in Figure 21. The profile of the curve is very similar to those of other metal-metalloid systems (66) and to that reported on the same alloy in a neutron analysis (14). The oscillatory nature is prominent and the second peak is split with a well-developed shoulder. This splitting is more pronounced than that reported in the neutron study (14) on the alloy, but the difference is mainly caused by the change in radiation used for analysis. In their X-ray and neutron analyses on Fe₈₀B₂₀, P. Lamparter et al. (66) showed a similar pronounced splitting in the X-ray analysis and not in the neutron analysis. The

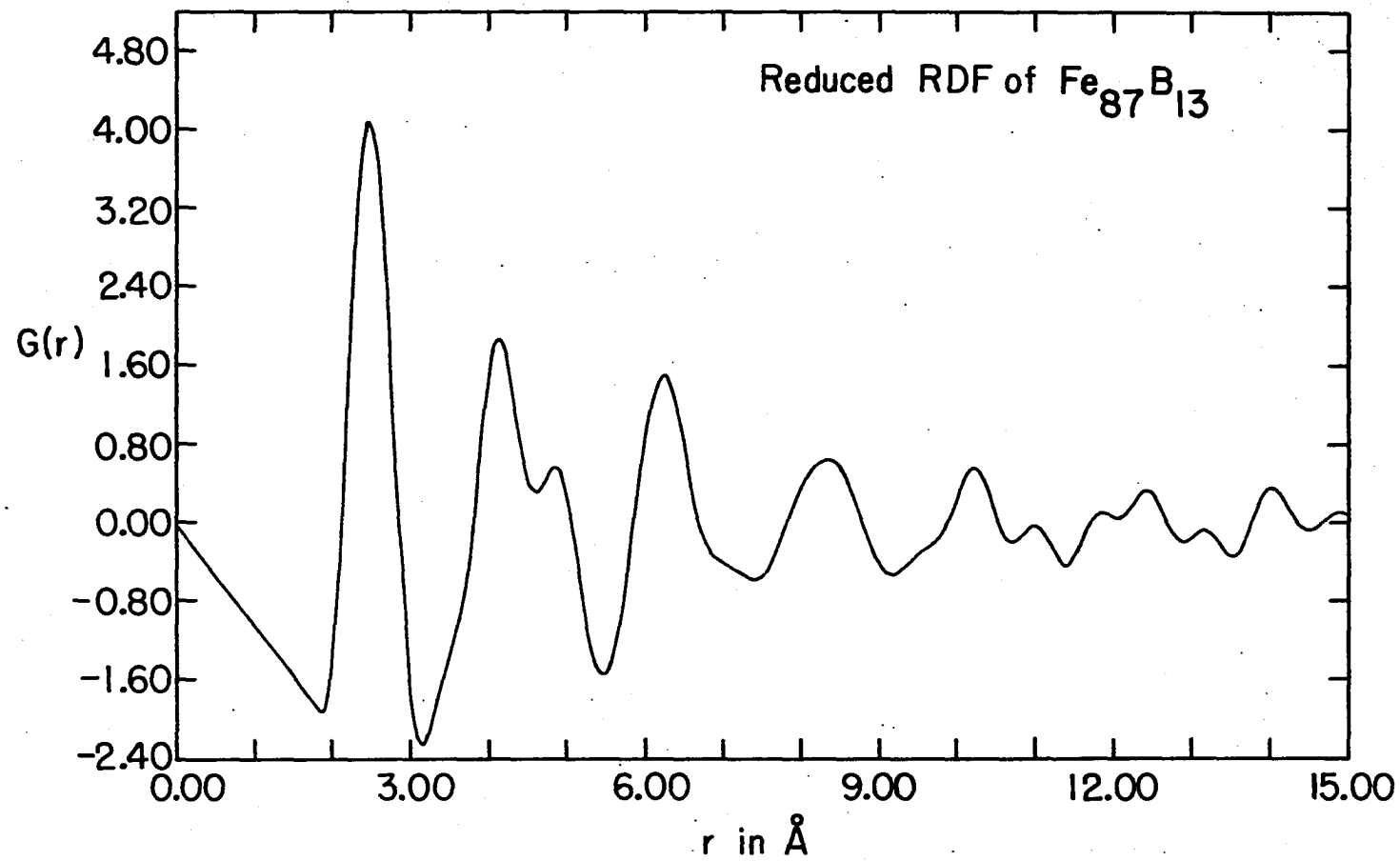


Figure 21. Reduced radial distribution function, $G(r) \equiv 4\pi r[\rho(r) - \rho_0]$, for Fe₈₇B₁₃. Positions of peaks indicate interatomic spacings

positions of the peaks and the ratios of the other peak positions to that of the first peak are listed in Table 5. The ratios are close to the values reported for these types of alloys. There is, however, a disagreement about the position of the first peak. We obtained $r_1=2.52\pm 0.05\text{\AA}$. Fukunaga et al. (15) reported $r_1=2.573\text{\AA}$ while Cowlam et al. (14) reported $r_1=2.52\text{\AA}$, but later published a revised value of $r_1=2.58\pm 0.05$ by normalizing the intensity of the first peak in the structure factor $S(k)$, using an average Fe moment of $2.1 \mu_B$ (14). In this type of Fourier transformation, as has been shown by Cargill (67), the position of the first peak in r -space is strongly dependent on the width, height, and position of the major peak, i.e., the first peak, in k -space. The result obtained in this work, although on the low side, is in agreement, within experimental error, with the values previously reported. (It should be noted that recently published EXAFS results (68) give $r_1=2.30\text{\AA}$ and a reconciliation of the results obtained by various RDF methods is definitely needed.)

The total number of nearest neighbors obtained from the area under the first maximum is 11.9 ± 0.2 , which is in very good agreement with the X-ray values reported for Fe-B alloys (16), but is lower than the neutron analysis result of 13.1 (14). Obtaining the nearest coordination number, n_1 , from the area under the symmetrical part of the first peak and designating the remaining area under the first peak as n_2 , according to a method previously proposed (15), we find that n_1 may be related to Fe-Fe pairs and n_2 related to Fe-B pairs. From Table 5, the values $n_1=10.6$ and $n_2=1.3$ agree very well with the $n_1=10.5$ and $n_2=1.4$ values reported (16).

A more serious controversy concerns the relative heights of the second peak and its shoulder. Waseda and Chen (16) have suggested that

Table 5. Nearest neighbors distances and ratios and number of nearest neighbors calculated from first peak in RDF

Alloys	r_1	r_2	r_3	r_4	r_5	r_2/r_1	r_3/r_1	r_4/r_1	d density g/cm ³	ρ_0 atom/A ⁻³	nearest neighbors			Ref. for d
											n	n_1	n_2	
Fe ₈₇ B ₁₃	2.52	4.18	4.90	6.29	8.35	1.66	1.94	2.50	7.48	0.0901	11.9	10.6	1.3	60
Fe ₈₂ B ₁₂ C ₆	2.52	4.15	4.89	6.30	8.45	1.65	1.94	2.50	7.40	0.0932	11.8	10.2	1.6	73
Fe ₈₂ B ₁₂ Si ₆	2.52	4.17	4.93	6.24	8.44	1.65	1.96	2.48	7.39	0.0913	12.2	10.3	1.9	81
Fe ₈₂ B ₁₄ Be ₄	2.51	4.14	4.89	6.28	8.34	1.65	1.95	2.50	7.35	0.0929	12.3	10.5	1.8	43
Fe ₈₂ B ₁₃ Be ₅	2.47	4.17	4.93	6.17	8.24	1.65	2.00	2.50	7.35	0.0929	12.2	9.1	3.1	43

for Fe-B alloys containing less than 20 at.% B, the subpeak in $G(r)$ is more intense than the second peak, i.e., a reversal of the situation usually found in most metal-metalloid system. This led them to support the original calculation by Bennett (69) of the dense random packing of hard sphere (DRPHS) model as being applicable to the structure of Fe-B and to reject the extended calculation based on the relaxed Bennett model (70) which gives the peaks heights in $G(r)$ more like those for Fe-B alloys with $B > 20$ at.% and that of $Fe_{83}P_{17}$ (16). The hard sphere Percus-Yevick model (71) also gives the shoulder as being more intense than the second peak. The results of Cowlam et al. (14) and the data presented in Figure 21, contradict the results and explanation of Waseda and Chen (16) since we find the subpeak to be lower than the second peak, thus supporting the relaxed Bennett model (70) with a starting nucleus of a tetrahedron, a dodecahedron, or an icosahedron (72), all of which duplicate the profile of our $G(r)$ curve.

2. $Fe_{82}B_{12}C_6$ and $Fe_{82}B_{12}Si_6$

The $G(r)$ curves for these two alloys are shown in Figures 22 and 23. The position of the first peak is not affected by the addition of C or Si to Fe-B at least up to 6 at.%. The effect of adding 6 at.% C to $Fe_{85}B_{15}$ at the expense of B has been studied by energy dispersive X-ray diffraction (EDXD) (73). The results are in agreement with ours in that no change in r_1 was observed, although r_1 was found to be 2.56\AA in the EDXD study. Our results also agree with those of Egami (73) in that the addition of C tends to reduce the intensity at the lower r side of the first peak and it also reduces the intensity of the second peak while

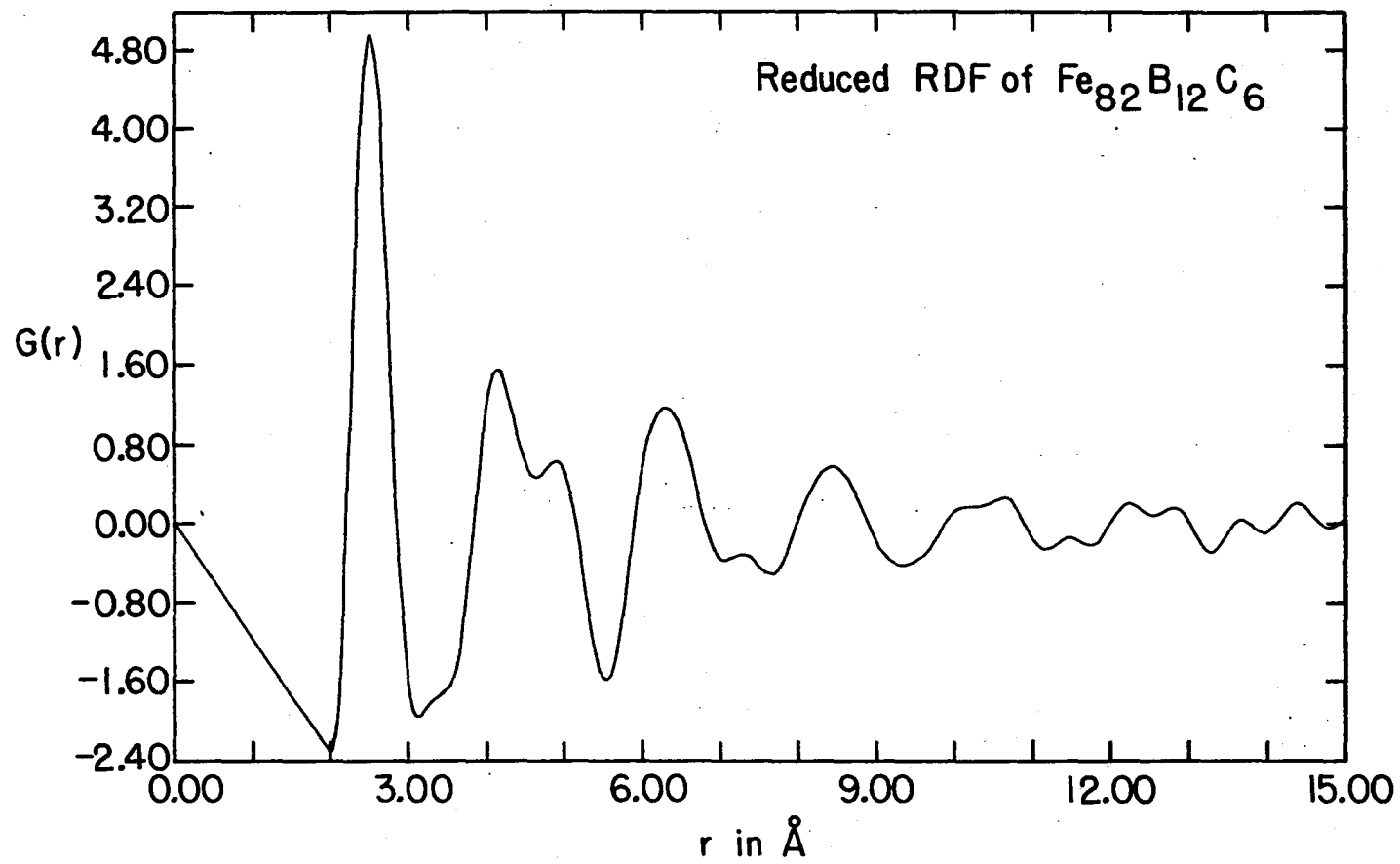


Figure 22. Reduced radial distribution function, $G(r)$ for $\text{Fe}_{82}\text{B}_{12}\text{C}_6$

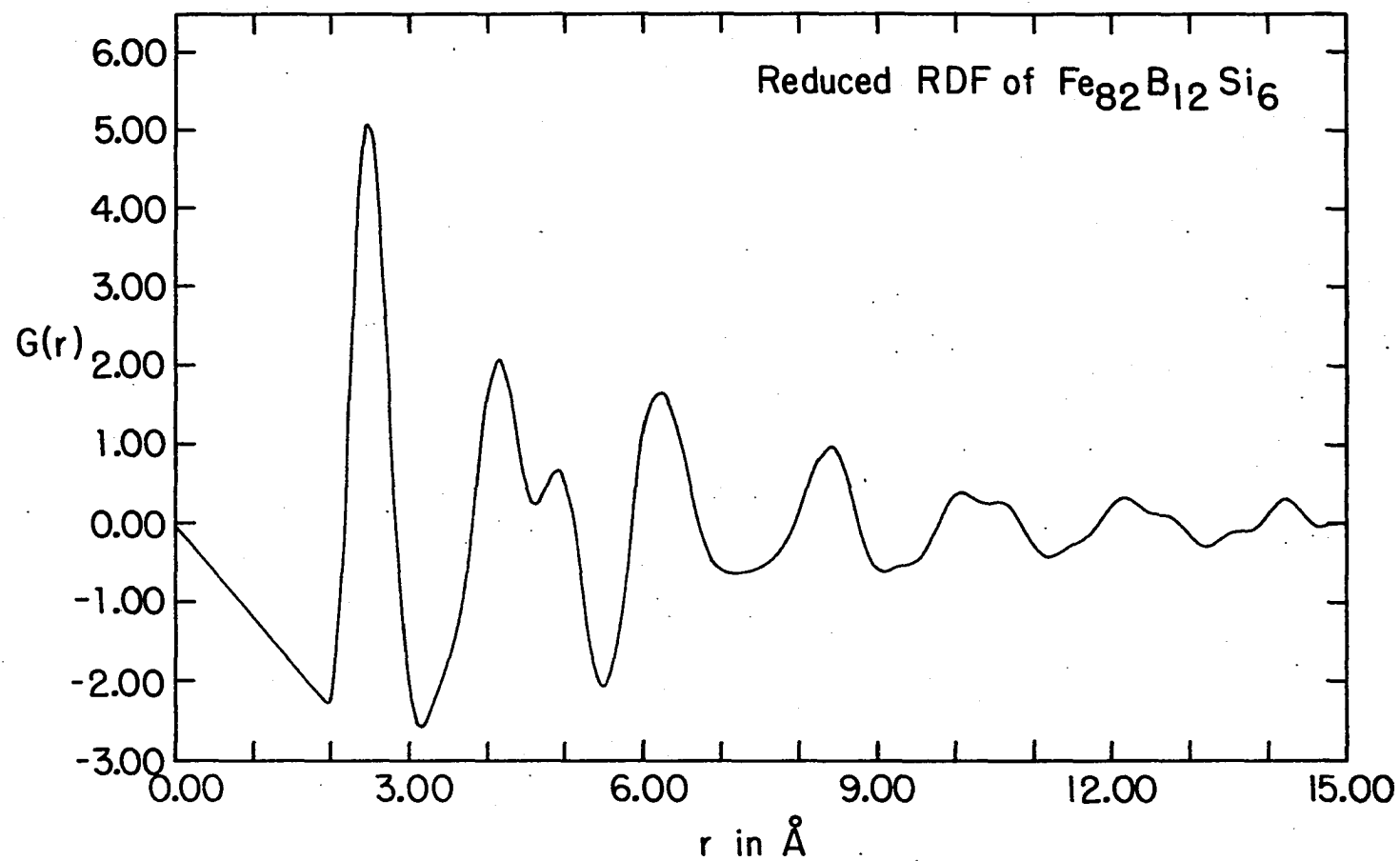


Figure 23. Reduced radial distribution function, $G(r)$ for $\text{Fe}_{82}\text{B}_{12}\text{Si}_6$

increasing that of the shoulder. There is also an increase in the intensity at the position of the valley between the second peak and its shoulder, thereby increasing the shallowness of the valley.

On the other hand, the addition of Si to $\text{Fe}_{82}\text{B}_{18}$ increases the intensity of the second peak and the intensity ratio of the peak to that of its shoulder has increased over that of $\text{Fe}_{87}\text{B}_{13}$ and $\text{Fe}_{82}\text{B}_{12}\text{C}_6$. Although there is some depletion of the intensity on the low r side of the first peak when compared to $\text{Fe}_{87}\text{B}_{13}$, the magnitude of the reduction is somewhat less than that of $\text{Fe}_{82}\text{B}_{12}\text{C}_6$. In general, the first maximum in each alloy is very similar. Therefore, it is not surprising that the number of nearest neighbors, derived from the areas under the peak is about the same (11.8 for $\text{Fe}_{82}\text{B}_{12}\text{C}_6$ and 12.2 for $\text{Fe}_{82}\text{B}_{12}\text{Si}_6$).

Caution must be exercised when one attempts to compare the RDF results from two different samples since sample geometry and experimental conditions, such as the intensity of the X-ray tube and detector alignment over the long counting period, may vary. One may lend more credence to differences observed when structural changes in the same sample are monitored by RDF. It is within this framework and constraint that the following discussion is given.

From the recent X-ray and neutron diffraction results on $\text{Fe}_{80}\text{B}_{20}$ by Lamparter et al. (66), the positions of the second peak and its shoulder reflect Fe-Fe nearest neighbor interactions. The increase in intensity of these peaks in the S alloys containing Si over that of the alloy containing C may support the idea that Si atoms occupy the Fe sites. Moreover, since the valley between the second peak and its shoulder is attributed to Fe-metalloid interactions (66), the higher intensity (the

less pronounced nature of the valley) of this region in the latter alloy may point to C atoms occupying the interstitial-like positions usually favored by the B atoms. The effect of the larger Si atoms occupying Fe sites and the smaller C atoms fitting in the interstices formed in the Fe DRPHS matrix is an increase in some Fe-Fe separations. This effect may be what is reflected in the depletion of the low r -side of the first peak in the $G(r)$ curves. Chen et al. (74) have argued that in some metallic glasses the exchange interaction, J , may be correlated to the interatomic distance of the transition metal, similar to the Bethe-Slater criterion for ferromagnetic spin coupling based on D/R , where $2R$ is the diameter of the 3d subshell and $D=2 \times r_1$ obtained from the peak positions in the $G(r)$ curves. Kloss (75) has argued and Egami supports the idea (73) that a Fe-Fe interatomic separation smaller than the average Fe-Fe separation of r_1 may lead to a negative exchange interaction for various Fe-Fe pairs. Conversely, an increase in Fe-Fe interatomic separation may decrease the number of negative exchange interactions.

In the Si- and C-substituted alloys, an increase in the room temperature saturation magnetization, M_s , over that of the corresponding binary Fe-B alloy is not expected since neither the M_s (4.2) nor the Curie temperature is significantly changed by the addition of C or Si (76-79). However, the change in B in the equation

$$M_s(T) = M_s(0) [1 - BT^{2/3} \dots] \quad (11)$$

is understandable when one considers the spin-wave stiffness coefficient, D . In the relation

$$B = \xi(3/2) g \mu_B / M(0) \left[\frac{k_B}{4\pi D} \right]^{3/2} \quad (12)$$

where $\xi(3/2)$ is the Bose-Einstein function equal to $0.0587(4\pi)^{3/2}$ and k_B is Boltzmann's constant, we see that $B \propto 1/D^{3/2}$.

The magnon dispersion relation at small values of the wave vector k in crystalline ferromagnets has the form (80)

$$E(k) \propto J a_0^2 k^2 \quad (13)$$

where a_0 is the lattice constant. This relation can be extended to non-crystalline ferromagnets by using a distribution of J and a_0 values in the form:

$$E(k) \propto J(1+\alpha) a_0^2 (1+\delta)^2 k^2. \quad (14)$$

Combining this relation with the quadratic dispersion relation for ferromagnetic magnons,

$$E(k) = Dk^2, \quad (15)$$

one may relate D to J in the following manner

$$D = J(1+\alpha) a_0^2 (1+\delta)^2 k^2 \quad (16)$$

for small values of k . Hence, if an increase in Fe-Fe interatomic separation is related to an increase in the average J value, the value of D is expected to increase. Recalling that $B \propto 1/D^{3/2}$ the value of B should decrease and this would be consistent with higher $M_s(T)$ values at room temperature in the ternary with C or Si even though the $M_s(0)$ values of the ternary alloys and the corresponding Fe-B binary alloy are essentially

the same.

3. Fe₈₂B₁₄Be₄ and Fe₈₂B₁₃Be₅

From Table 6 and from the $G(r)$ curves displayed in Figures 24 and 25, one can see certain distinct differences between these two Be-substituted alloys. The addition of a third element to Fe-B alloys does not usually affect the position of the Fe-Fe peak within this composition range (67). Therefore, the change in r_1 from 2.51Å for Fe₈₂B₁₄Be₄ to 2.47Å for Fe₈₂B₁₃Be₅ should be considered a very pronounced shift. Also, this is not merely a change in the shape of one side of the peak, but a shift in the position of the maximum and its related distribution of interatomic distances with their corresponding probabilities. It should be recalled that a dramatic shift was observed for these two alloys in the Auger results which indicated that for Fe₈₂B₁₄Be₄, Be appeared to have transferred its outer electrons while for Fe₈₂B₁₃Be₅, no such transfer could be inferred. The magnetization measurements also indicated that the average Fe moment in Fe₈₂B_{18-x}Be_x increased for $x \leq 4$, but decreased for $x > 4$. These changes can be reconciled with the structural changes, as is described below.

The magnetic behavior of Fe is very sensitively dependent on the Fe-Fe separation and the Fe moment observed is an average value. In fcc Fe, a shift of the lattice constant from 3.64Å to 3.54Å, which corresponds to a shift in interatomic spacing from 2.57Å to 2.50Å, has been shown to be responsible for, or coincidental with, a change from a ferromagnetic spin structure with moment of about 2.9 μ_B to an antiferromagnetic spin structure with moment of 0.7 μ_B (11, 12).

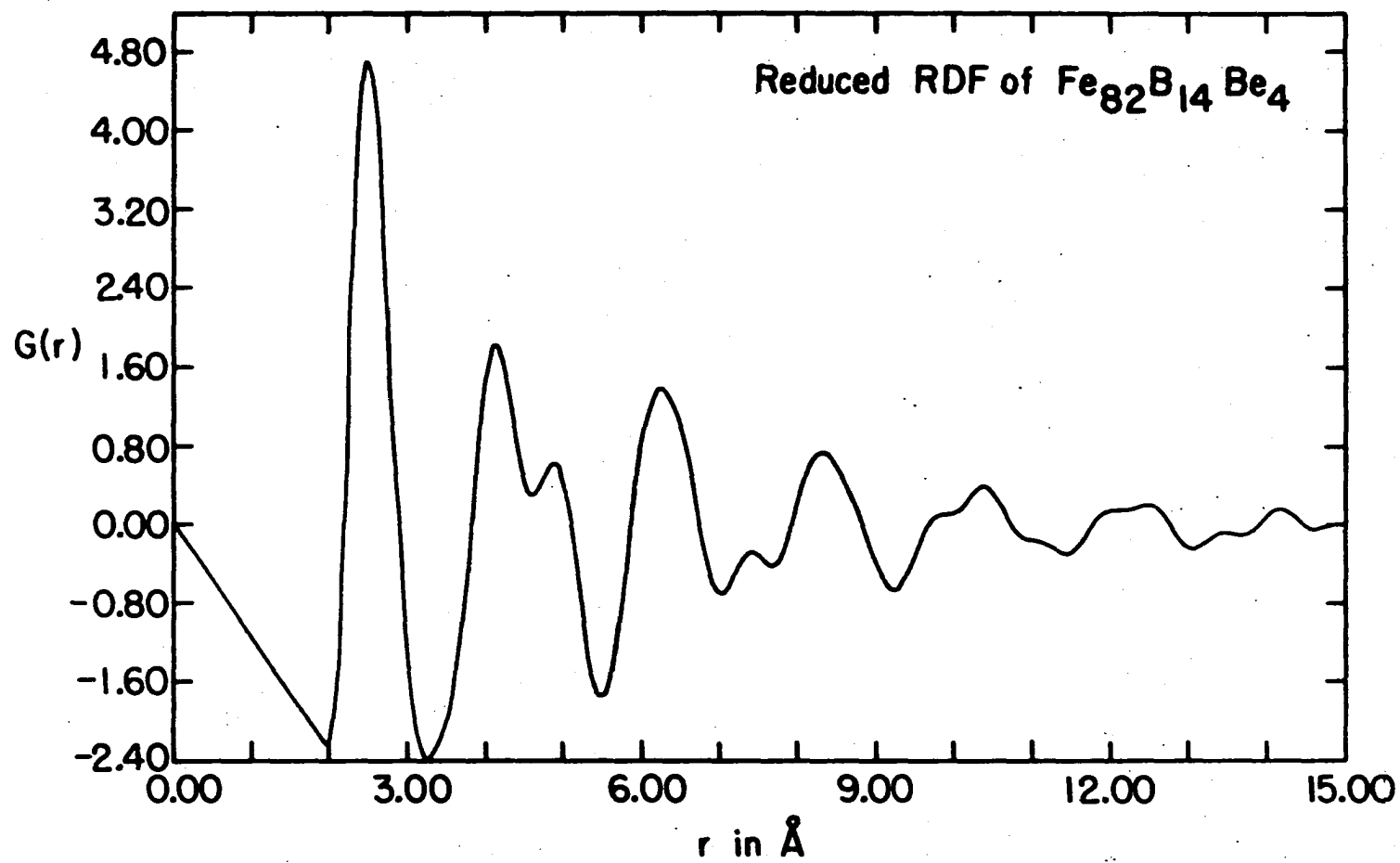


Figure 24. Reduced radial distribution function, $G(r)$ for $\text{Fe}_{82}\text{B}_{14}\text{Be}_4$

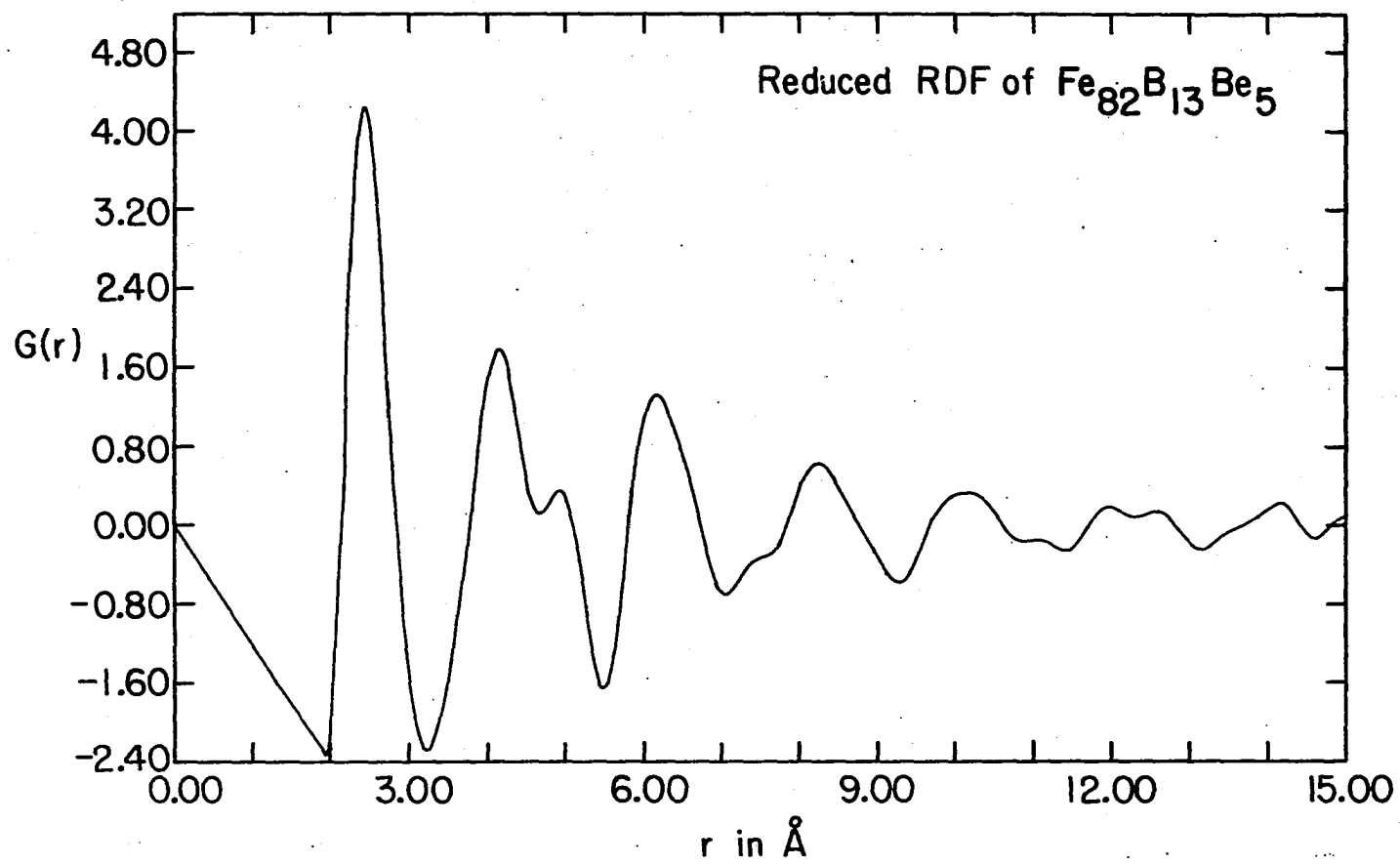


Figure 25. Reduced radial distribution function, $G(r)$ for $\text{Fe}_{82}\text{B}_{13}\text{Be}_5$

It is therefore possible to relate the shift in the position of the peak in the amorphous Fe-base alloys to the change in the average Fe magnetic moment. First, one must note that an amorphous structure is an assembly of atoms at various distances with respect to an arbitrary origin. There is a variety of Fe-Fe interactions within the distances covered by the first peak. A shift in the position of the maximum of the peaks (r_1) to a lower r value without a significant change in the shape of the peak lowers the probability (i.e., lowering the number) of Fe-Fe interactions occurring at large r values and an increase in Fe-Fe interactions at r values less than r_1 . If we assume that Fe-Fe pairs with spacing less than r_1 have negative exchange interaction ($J < 0$) (74, 75), then the decrease in the average Fe moment in $\text{Fe}_{82}\text{B}_{13}\text{Be}_5$ may mean a change of some ferromagnetic spin interaction to antiferromagnetic spin interaction.

The large change in n_1 from 10.5 to 9.1 as the Be content is increased from 4 to 5 at.% (see Table 6) is very surprising, but yet is consistent with a decrease in the average Fe moment, $\bar{\mu}_{\text{Fe}}$. Fukunaga et al. (15) have shown that in $\text{Fe}_{100-x}\text{B}_x$ alloys the n_1 values and $\bar{\mu}_{\text{Fe}}$ both go through a maximum at $x \approx 14$. The magnitude of the change in n_1 ($\Delta n_1 = -1.4$) is greater in these ternary alloys, but this dramatic shift is consistent with the other discontinuous behavior of $\text{Fe}_{82}\text{B}_{18-x}\text{Be}_x$ in the range of $x=4$ and 5. The change in n_2 ($\Delta n_2 = +1.3$) is also worth noting. If we assume that in $\text{Fe}_{82}\text{B}_{13}\text{Be}_5$ Fe has lost some Fe first nearest neighbors and some Be atoms are now residing in a nearest neighbor shell with $r_{\text{Fe-Be}} < r_{\text{Fe-Be}}$ of $\text{Fe}_{82}\text{B}_{14}\text{Be}_4$, we can understand how it is possible to have Fe-Be bonding interaction. The fact that the $r_{\text{Fe-Fe}}$ is somewhat less

than the Fe Goldschmidt diameter of 2.49\AA may point to loss of outer electrons from the Fe atoms. The isomer shift from the Mössbauer spectroscopy study shows a decrease which may be interpreted as an increase in the 3s electron density around the Fe nucleus, probably caused by the lessening of the screening by the outer electrons, some of which may be participating in the Fe-Be bonding interaction.

The decrease in the Curie temperature, T_C , when x goes from 4 to 5 can be explained in terms of the expression

$$3k_B T_C = 2zS(S+1) J_{\text{Fe-Fe}} \quad (17)$$

where z is the number of nearest neighbors. Since $J_{\text{Fe-Fe}}$ and z decrease, T_C should also decrease.

V. SUMMARY AND CONCLUSIONS

The partial substitution of divalent Be for trivalent B in amorphous $\text{Fe}_{82}\text{B}_{18}$ was shown to cause an initial increase and subsequent decrease in the average Fe moment. The Curie temperature, T_C , decreased monotonically. The reversing effect in the average Fe moment caused by Be was confirmed by measurements of Auger electron and Mössbauer spectroscopies. The Auger results indicated that for $x \leq 4$ in $\text{Fe}_{82}\text{B}_{18-x}\text{Be}_x$ there appears to be a transfer of charge from Be, probably to Fe. At higher Be contents no such charge transfer could be inferred. From the Mössbauer study, the effective hyperfine field initially increased for $x \leq 4$, but decreased for $x > 4$. The isomer shift changed from -0.032 mm/sec to -0.050 mm/sec for the same change in the Be content.

The annealing behavior of the $\text{Fe}_{82}\text{B}_{18-x}\text{Be}_x$ alloys was studied by both X-ray and Mössbauer spectroscopies. For the binary alloy $\text{Fe}_{82}\text{B}_{18}$, the crystallization products at 693K were identified as tetragonal Fe_3B and α -Fe. Additions of Be produced two crystallization stages. The crystallization products of the first stage were a solid solution of α -Fe-Be and a metastable amorphous phase containing more B than the concentration in the as-quenched ribbons. At the second stage, Fe_2B was observed to precipitate out. The intensity ratios in the Mössbauer spectra and the d-spacings deduced from the X-ray data indicated that the Be content in the Fe-Be solid solution at the second annealing stage was 4-5 at.% in all the Be alloys. The Mössbauer spectra clearly indicated that annealing the samples at a temperature between the two stages led to the alignment of the effective magnetic hyperfine field, \bar{H}_{eff} , almost parallel to the

plane of the ribbon, while annealing above the second stage caused \bar{M}_{eff} to be randomly oriented probably because of the absence of lattice strain.

Radial distribution function analyses conducted on $\text{Fe}_{82}\text{B}_{14}\text{Be}_4$ and $\text{Fe}_{82}\text{B}_{13}\text{Be}_5$ indicated that the interatomic distance of Fe-Fe atom pairs, $r_{\text{Fe-Fe}}$, decreased from 2.51Å to 2.47Å while the number of first nearest neighbors, n_1 , decreased from 10.5 to 9.1 when the Be content is increased from 4 to 5 at.%. All the results indicate a significant change in the Fe nearest neighbor environment between $x=4$ and $x=5$. The increase in the average Fe moment is explained on the basis of an initial transfer of charge from Be to Fe, replacing the d electrons that are participating in a new Fe-B hybrid bonding orbital. The subsequent decrease in the Fe moment is explained in terms of: (1) an increase in the number of negative exchange interactions due to the smaller Fe-Fe interatomic spacings and (2) the absence of charge transfer from Be to Fe. Also, the reduction in n_1 and $r_{\text{Fe-Fe}}$ when the Be content is increased from 4 to 5 at.% is correlated with the observed decrease in T_C .

Additions of Au to Fe-B resulted in an average Fe moment of 2.20 μ_B in $\text{Fe}_{82}\text{B}_{16.5}\text{Au}_{1.5}$ and 2.46 μ_B in $\text{Fe}_{87}\text{B}_{11}\text{Au}_2$. The ternary alloy with 0.5 at.% Au displayed two crystallization stages with a solid solution of Fe-Au precipitating at the first stage and the intermetallic compound Fe_2B forming at the second stage. Higher additions of Au produced a third stage at which an Au-rich solid solution was precipitated. The annealing of $\text{Fe}_{87}\text{B}_{11}\text{Au}_2$ resulted in lower M_S , unlike the annealing effect usually observed in Fe-base metallic glasses. This behavior of $\text{Fe}_{87}\text{B}_{11}\text{Au}_2$ was explained in terms of a reduction in the Fe-Fe interatomic distance and its attendant effect on the Fe moment.

The RDF analyses on $\text{Fe}_{82}\text{B}_{12}\text{C}_6$ and $\text{Fe}_{82}\text{B}_{12}\text{Si}_6$ indicated that the higher saturation magnetization at room temperature of these two ternary alloys, compared to that of Fe-B alloys, is probably due to an increase in the spin-wave stiffness constant.

VI. BIBLIOGRAPHY

1. R. C. O'Handley, R. Hasegawa, R. Ray and C-P. Chou, J. Appl. Phys. 48, 2095 (1977).
2. N. Lundquist, H. P. Myers and R. Westin, Phil. Mag. 7, 1198 (1962).
3. R. C. O'Handley and D. S. Boudreaux, Phys. Stat. Sol. (A) 45, 607 (1978).
4. N. S. Kazama, T. Masumoto and M. Mitera, J. Magn. and Magn. Mat. 15-18, 1331 (1980).
5. N. S. Kazama, M. Mitera and T. Masumoto, in Rapidly Quenched Metals III, vol. 2 (The Metals Society, London, 1978), p. 164.
6. A. M. Baró, M. Salmeron and J. M. Rojo, J. Phys. F 5, 826 (1975).
7. C. L. Chien, Phys. Rev. 18, 1003 (1978).
8. T. Kémény, I. Vincze, B. Fogarassy and Sigurds Arajcs, Phys. Rev. B 20, 476 (1979).
9. W. Felsch, Z. Angew. Phys. 29, 217 (1970).
10. M. F. Collins and B. Forsyth, Phil. Mag. 8, 401 (1963).
11. L. Kaufman, E. V. Clougherty and R. J. Weiss, Acta Metall., 11, 323 (1963).
12. J. G. Wright, Phil. Mag. 24, 217 (1971).
13. J. G. Wright, IEEE Trans. Magn. MAG-12, 95 (1976).
14. N. Cowlam, H. A. Davies and K. Dini, J. Non-Cryst. Solids 40, 377 (1980).
15. T. Fukunaga, M. Misawa, K. Fukamichi, T. Masumoto and K. Suzuki, in Rapidly Quenched Metals III, vol. 2 (The Metals Society, London, 1978), p. 325.
16. Y. Waseda and H. S. Chen, Phys. Stat. Solidi (A) 49, 387 (1978).
17. R. Hasegawa and R. Ray, J. Appl. Phys. 49, 4174 (1978).
18. L. E. Davis, N. C. MacDonald, P. W. Palmberg, G. E. Riach and R. E. Weber, Handbook of Auger Electron Spectroscopy (Physical Electronics Industries, Eden Prairie, Minnesota, 1976).

19. H. P. Klug and L. E. Alexander, X-ray Diffraction Procedures (John Wiley & Sons, New York, 1974), Chapter 12.
20. C. N. J. Wagner, J. Non-Cryst. Solids 42, 3 (1980).
21. R. Kaplow, S. L. Strong and L. L. Averbach, Phys. Rev. 138, A1336 (1965).
22. C. W. Chen, Magnetism and Metallurgy of Soft Magnetic Materials (North Holland, Amsterdam, 1977), p. 100.
23. C. D. Graham, Jr. and T. Egami, Ann. Rev. Mater. Sci. 8, 423 (1978).
24. W. B. Pearson, A Handbook of Lattice Spacings of Metals and Alloys Vol. I, (Pergamon Press, London, 1964), p. 633.
25. D. M. Zehner, Noel Barbulesco and L. H. Jenkins, Surf. Sci. 34, 385 (1973).
26. R. Jennison and H. H. Madden, Phys. Rev. B 21, 430 (1980).
27. M. Suleman and E. B. Pattinson, J. Phys. F 3, L53 (1978).
28. D. R. Jennison, Phys. Rev. B 18, 6996 (1978).
29. C. L. Chien and H. S. Chen, J. Phys. Coll. 40C2, 118 (1979).
30. T. Moriya, J. Magn. and Magn. Mat. 14, 1 (1979).
31. B. Window, J. Phys. E 4, 401 (1971).
32. C. L. Chien, Phys. Rev. B 19, 81 (1979).
33. P. J. Schurer and A. H. Morrish, Solid State Comm. 28, 819 (1978).
34. I. Vincze, M. C. Cadeville, R. Jesser and J. Takacs, J. Phys. 35, C6-533 (1974).
35. H. N. Ok and A. H. Morrish, Phys. Rev. B 22, 4215 (1980).
36. M. C. Lin, C. S. Severin, R. G. Barnes and C. W. Chen, to be published in Phys. Rev. B.
37. C. L. Chien, D. Musser, F. E. Luborsky and J. L. Walter, J. Phys. F 8, 2407 (1978).
38. C. L. Chien, D. Musser, E. M. Gyorgy, R. C. Sherwood, H. S. Chen, F. E. Luborsky and J. L. Walter, Phys. Rev. B 20 283 (1979).
39. H. Bernas, I. A. Campbell and R. Fruchart, J. Phys. Chem. Solids 28, 17 (1967).

40. Y. Nakamura, IEEE Trans. Magn. MAG-12, 278 (1978).
41. J. Dorion, J. Chem. Phys. 39, 236 (1963).
42. C. S. Severin, C. W. Chen, A. J. Bevolo and M. C. Lin, J. Appl. Physics 52, 1850 (1981).
43. R. Hasegawa, J. Appl. Phys. 52, 1847 (1981).
44. G. K. Wertheim, V. Jaccarino, J. H. Wernick and D. N. E. Buchanan, Phys. Rev. Lett. 12, 24 (1964).
45. I. Vincze and A. T. Aldred, Solid State State Comm. 17, 639 (1975).
46. I. Vincze and A. T. Aldred, Phys. Rev. B 9, 3845 (1974).
47. H. N. Ok and A. H. Morrish, Phys. Rev. B 22, 3471 (1980).
48. M. Matsuura, T. Nomoto, F. Itoh and K. Suzuki, Solid State Comm. 33, 895 (1980).
49. K. Terakura and J. Kanamori, Prog. Theor. Phys. 46, 1007 (1967).
50. Y. Fukai, S. Kazama, K. Tanaka and M. Masumoto, Solid State Comm. 19, 507 (1976).
51. L. Takacs, Phys. Stat. Sol. (A) 56, 371 (1979).
52. J. D. Corbett and J. W. Anderegg, Inorg. Chem. 19, 3822 (1980).
53. L. Pauling, Proc. Roy. Soc. A196, 343 (1949).
54. P. J. Brown and J. L. Cox, Phil. Mag. 23, 705 (1971).
55. R. Alben, J. I. Budnick and G. S. Cargill, III, in Metallic Glasses (ASM, Metals Park, Ohio, 1977), Chapter 12.
56. A. C. Switendick, Solid State Comm. 19, 511 (1976).
57. C. W. Chen, Magnetism and Metallurgy of Soft Magnetic Materials (North Holland, Amsterdam, 1977), p. 196.
58. A. J. Bevolo, C. S. Severin and C. W. Chen, submitted to Phys. Rev. Lett.
59. R. Ray, R. Hasegawa, C-P. Chou and L. A. Davis, Scr. Met. 11, 973 (1977).
60. M. Mehra, E. C. Subbarao, P. C. Kapur and R. Hasegawa, IEEE Trans. Magn. MAG-16, 1141 (1980).

61. F. E. Luborsky, J. J. Becker, J. L. Walker and H. H. Liebermann, *IEEE Trans. Magn.* MAG-15, 1146 (1979).
62. H. Hiroyoshi, K. Fukamichi, M. Kikuchi, A. Hoshino and T. Masumoto, *Phys. Lett.* 65A, 163 (1977).
63. M. W. Ruckmon, R. A. Levy, A. Kessler and R. Hasegawa, *J. Non-Cryst. Solids* 40, 393 (1980).
64. G. Marchal, Ph. Mangin and Chr. Janot, *Phil. Mag.* 32, 1007 (1975).
65. W. B. Pearson, *A Handbook of Lattice Spacings of Metals and Alloys, Vol. I*, (Pergamon Press, London, 1964), p. 424.
66. P. Lamparter, E. Nold, G. Rainer-Harbach, E. Grallath and S. Steeb, *Z. Naturf.* 36A, 165 (1981).
67. G. S. Cargill, III, *Solid State Phys.* 30, 227 (1975).
68. M. De Crescenzi, A. Balzarotti, F. Comin, L. Incoccia, S. Mobilio and N. Motta, *Solid State Comm.* 37, 921 (1981).
69. C. H. Bennett, *J. Appl. Phys.* 43, 272 (1972).
70. L. V. Heimendahl, *J. Phys. F* 5, L141 (1975).
71. G. J. Throup and P. J. Bearman, *J. Chem. Phys.* 42, 2408 (1965).
72. T. Ichikawa, *Phys. Stat. Sol. (A)* 29, 293 (1975).
73. T. Egami, *J. Appl. Phys.* 50, 1564 (1979).
74. H. S. Chen, R. C. Sherwood and E. M. Gyorgy, *IEEE Trans. Magn.* MAG-13, 1538 (1977).
75. R. Kloss, *Int. J. Magn.* 5, 251 (1973).
76. J. Balogh, I. Dèzsi, B. Forgarassy, L. Grànàssy, D. L. Nagy, I Vincze and S. Arajcs, *J. de Phys. (Paris)* 41, C253 (1980).
77. S. Hatta and T. Egami, *J. Appl. Phys.* 50, 1589 (1979).
78. F. E. Luborsky, J. J- Becker, J. L. Walter, D. L. Martin, *IEEE Trans. Magn.* MAG-16, 521 (1980).
79. F. E. Luborsky and J. L. Walter, *IEEE Trans. Magn.* MAG-16, 572 (1980).
80. C. L. Chien and R. Hasegawa, *Phys. Rev. B* 16, 2115 (1977).

81. F. E. Luborsky, P. G. Frischmann and L. A. Johnson, *J. Magn. and Magn. Mat.* 19, 130 (1980).

VII. ACKNOWLEDGMENTS

I wish to express my appreciation to Professor C. W. Chen for having had the opportunity to work with him. His scientific guidance and his allowing me the latitude to exercise my curiosity were valuable.

I would like to acknowledge the collaboration of Mou C. Lin in the Mössbauer spectroscopy study and Al J. Bevolo in the Auger electron spectroscopy study. My thanks go to Professor C. N. J. Wagner of UCLA; to Jim Benson, Barb Helland, and Professor Robert Jacobson of the X-ray group; to Fran Laabs for his help in electron microscopy and microprobe analysis; to Tom Naig and Wes Alexander for their friendship and help in the machine shop; to Wayne Buttry and P. B. V. Narayan for helpful discussion; to my sister Patricia and Jerry Tilden for helping from the beginning to the end; and to Rose Bielefeldt for typing of the manuscript.

I am especially thankful to Elizabeth for her encouragement.